



Calhoun: The NPS Institutional Archive

Faculty and Researcher Publications

Faculty and Researcher Publications Collection

2016-12-16

On the plasma-based growth of 'flowing' graphene sheets at atmospheric pressure conditions

Tsyganov, D.

IOP Publishing Ltd

Tsyganov, D., et al. "On the plasma-based growth of 'flowing' graphene sheets at atmospheric pressure conditions." *Plasma Sources Science and Technology* 25.1



Calhoun is a project of the Dudley Knox Library at NPS, furthering the precepts and goals of open government and government transparency. All information contained herein has been approved for release by the NPS Public Affairs Officer.

Dudley Knox Library / Naval Postgraduate School
411 Dyer Road / 1 University Circle
Monterey, California USA 93943

<http://www.nps.edu/library>

On the plasma-based growth of ‘flowing’ graphene sheets at atmospheric pressure conditions

D Tsyganov¹, N Bundaleska⁶, E Tatarova¹, A Dias¹, J Henriques¹, A Rego²,
A Ferrara², M V Abrashev³, F M Dias¹, C C Luhrs⁴ and J Phillips⁵

¹ Instituto de Plasmas e Fusão Nuclear, Instituto Superior Técnico, Universidade de Lisboa, Portugal, 1049-001 Lisbon, Portugal

² Centro de Química-Física Molecular and IN, Instituto Superior Técnico, Universidade de Lisboa, 1049-001 Lisbon, Portugal

³ Faculty of Physics, University of Sofia, 1164 Sofia, Bulgaria

⁴ Mechanical and Aerospace Engineering Department, Naval Postgraduate School, Monterey, CA 93943, USA

⁵ Physics Department, Naval Postgraduate School, Monterey, CA 93943, USA

⁶ Formerly with Instituto de Plasmas e Fusão Nuclear, Instituto Superior Técnico, Universidade de Lisboa, 049-001 Lisbon, Portugal

E-mail: e.tatarova@ist.utl.pt

Received 19 March 2015, revised 30 August 2015

Accepted for publication 15 September 2015

Published 16 December 2015



CrossMark

Abstract

A theoretical and experimental study on atmospheric pressure microwave plasma-based assembly of free standing graphene sheets is presented. The synthesis method is based on introducing a carbon-containing precursor (C_2H_5OH) through a microwave (2.45 GHz) argon plasma environment, where decomposition of ethanol molecules takes place and carbon atoms and molecules are created and then converted into solid carbon nuclei in the ‘colder’ nucleation zones. A theoretical model previously developed has been further updated and refined to map the particle and thermal fluxes in the plasma reactor. Considering the nucleation process as a delicate interplay between thermodynamic and kinetic factors, the model is based on a set of non-linear differential equations describing plasma thermodynamics and chemical kinetics. The model predictions were validated by experimental results. Optical emission spectroscopy was applied to detect the plasma emission related to carbon species from the ‘hot’ plasma zone. Raman spectroscopy, scanning electron microscopy (SEM), and x-ray photoelectron spectroscopy (XPS) techniques have been applied to analyze the synthesized nanostructures. The microstructural features of the solid carbon nuclei collected from the colder zones of plasma reactor vary according to their location. A part of the solid carbon was deposited on the discharge tube wall. The solid assembled from the main stream, which was gradually withdrawn from the hot plasma region in the outlet plasma stream directed to a filter, was composed by ‘flowing’ graphene sheets. The influence of additional hydrogen, Ar flow rate and microwave power on the concentration of obtained stable species and carbon–dicarbon was evaluated. The ratio of sp^3/sp^2 carbons in graphene sheets is presented. A correlation between changes in C_2 and C number densities and sp^3/sp^2 ratio was found.

Keywords: microwave plasma, graphene, ethanol, carbon

 Online supplementary data available from stacks.iop.org/PSST/25/015013/mmedia

(Some figures may appear in colour only in the online journal)

1. Introduction

Carbon, which is one of the most abundant elements on Earth and plays an essential role in the ecosystem, has recently generated a renewed interest in the scientific community as new materials are being introduced and new applications for them become a reality. Carbon materials are of great interest for investigation and industrial activities owing to their abundance, stability and relative environmental friendliness [1–4]. Depending on the foreseen application, different carbon-based nanomaterials such as nanocrystals, fullerenes, carbon nanotubes (CNT), nanofibers, graphene, nanoribbons, and nanoflakes have been intensively investigated [4–18]. CNTs discovery symbolizes a benchmark in nanoscience [14].

Recently many research groups shifted their research target towards graphene and related structures (graphene sheets, nanoribbons, carbon nanowalls etc) due to their extraordinary properties and enormous potential for applications [1–3, 5–18]. The production of graphene requires specific conditions such as sufficiently high energy of the particles supplied to the growth zone and balanced influx of carbon particles. In the conventional chemical vapor deposition process, these conditions are met by the use of very high temperatures (~1000°C). Different carbon structures can be grown, depending on the catalyst nature and size, gas mixture and substrate temperature [3, 17, 18]. However to avoid the use of a catalyst and to improve the synthesis process, in terms of controllability, yield and quality of the nanostructures, a search for new methods is needed. In this respect, it is now well recognized that plasma environments constitute powerful tools in material science, by allowing the creation of advanced nanomaterials and the enhancement of long-existing materials that would not be otherwise achievable. Plasmas can ensure simultaneously high temperatures, highly reactive environment—electrons, ions, free radicals, energetic photons (UV radiation). For example, it has been shown that in plasma-enhanced chemical vapor deposition [1, 3, 5, 7, 9, 10] a high level of control over material fluxes, heating and concomitantly the structure and properties of formulated materials can be achieved. This method makes use of a substrate inserted in a low-pressure plasma environment. Thus, the synthesis and growth of carbon nanostructures proceed via surface reaction and therefore depend on surface conditions. The review of the current status of the plasma-based fabrication of carbon nanostructures and in particular of graphene can be found elsewhere [1, 3, 5, 9, 10]. Different plasma sources have been tested using various precursors (methane, alcohols, etc) for graphene synthesis [3, 10].

Many applications require nanosheets in the form of free-standing graphene flakes consisting of a few atomic monolayers. Such self-standing graphene sheets are alternative to horizontal graphenes supported by solid surfaces because they have an obvious advantage related to the fact that both surfaces and at least three open edges can be utilized in applications while surface-bound counterparts effectively use one surface. In this respect, a new approach for a large-scale fabrication of graphene flakes in magnetically enhanced dc arc discharge is presented by Levchenko et al [10]. The graphene

flakes are produced using a carbon anode, which is a rod with a hole in the center. The use of catalyst in this case should be mentioned, as the hole is filled with a mixture of graphitic carbon and catalyst (Y-Ni powder). Furthermore, current advancements demonstrate that self-standing graphene sheets can also be produced using plasmas at atmospheric pressure conditions. Microwave plasma processing via the so-called aerosol-through-plasma (A-T-P) technique has been used to produce a multitude of nanostructures, including graphene, that are of interest in many fields [9, 19–23]. In this technique, precursors, which can be solids, liquids or gases, are carried through hot microwave plasma where they decompose and species created are carried in the cold outlet plasma gas streams where nucleation and growth processes take place.

Plasma-based fabrication of graphene is a relatively new area with a relatively small number of publications [3, 10, 22–28]. Moreover, the mechanisms responsible for the unique properties exhibited by plasma-created nanostructures are still to be understood. Most of the results are obtained by applying phenomenological approaches. To achieve predetermined outcomes and reduce the trials to a minimum, it is of utmost importance to reveal the strong correlation existing between plasma features and material properties. However, relating the plasma-specific processes/features and specific structural qualities of assembled nanostructures that determine their electronic, mechanical, photonic, etc properties is a major challenge and one of the key goals in the plasma nanoscience research field. To this end, reliable numerical models that are validated by *in situ*—obtained experimental results can serve as powerful tools for mastering the synthesis and engineering processes. It should be well known how to channel the power into the targeted reactions and precursor species and how to control the energy exchange pathways in plasmas in an effort to provide sophisticated management of particles and energy fluxes towards the growing nanostructures.

These models, as a rule, should include reliable description of fluid mechanics and thermodynamics, i.e. nonequilibrium energy transport and species mass transport, plasma kinetics that includes processes resulting in formation of excited species and radicals and plasma chemistry. The processes of formation of solid nuclei, growth and interaction of plasma species with solid surfaces should be an integral part of such comprehensive modeling. Ideally, all these parts should be considered self-consistently in order to achieve a reliable description of the nanostructure growth dynamics and develop predictive capabilities about properties of assembled structures as a function of externally controllable parameters. Unfortunately, such a comprehensive simulation of plasma-based synthesis of carbon nanostructure, and graphene in particular, is not yet available. Nevertheless, it is possible to model some of the above-mentioned components of such integral model while considering others as black boxes. Such simplified models associated with particular aspects of the process can be instrumental for mastering the overall process of synthesis. For example, plasma chemistry modeling can give information about precursor's fluxes toward growing nanostructures, while plasma thermodynamics outputs are related to energy fluxes. The interaction of plasmas with

growing nanostructures can be simulated by applying phenomenological models or by detailed atomistic description of the processes of nucleation and growth using the results from plasma chemistry modeling as an input. A survey on different modeling efforts in the literature about plasmas used for carbon nanostructure synthesis is presented in Bogaerts *et al* [29]. The existing modeling approaches, such as analytical models, zero-dimensional (0D) chemical-kinetics simulations, fluid models (describing the chemical kinetics as well as fluid dynamics), solving the Boltzmann transport equation, and Monte Carlo (MC) are discussed. A multiscale computational framework (MSCF) incorporating a computational fluid dynamics software for reactor-scale processes, a kinetic MC solver for the growth of molecular structures and a molecular dynamic simulator for the self-assembly of atoms into molecular structures are some of the examples found in the literature [30, 31]. Multiscale simulations of carbon nanotube (CNT) nucleation and growth, supported by a catalyst (Ni, Co, and Fe), with coupled heat and mass flow is presented by Pannala and Wood [32]. Carbon diffusion, as well as the size and shape of the catalytic particles, were found to influence the CNT growth rate. However, no investigation on the bulk formation of carbon nanoparticles was conducted.

The present complex theoretical and experimental investigation is a continuation of our previous work [27, 28] on the creation of self-standing graphene sheets using microwave atmospheric plasmas driven by surface waves at atmospheric pressure conditions. The method, as described previously [27, 28], is based on injecting a carbon-containing precursor (C_2H_5OH) through a microwave argon plasma environment, where decomposition of ethanol molecules takes place and carbon atoms and molecules are created. Gas-phase carbon species diffuse into colder nucleation zones, where they are transformed into solid carbon nuclei. Aiming at further elaboration of the method and replacement of the phenomenological approach with a deterministic one, a theoretical model previously developed has been further updated and refined to describe in detail the formation of carbon precursor species and the creation of solid carbon nuclei.

Taking into consideration that the nucleation process is an interplay between thermodynamic and kinetic factors, the model is based on a set of nonlinear spatially dependent differential equations describing plasma thermodynamics and chemical kinetics. Considering the diffusion of carbon species into colder zones of plasma reactor, the formation of solid carbon nuclei is analyzed in detail. A fraction of the produced solid carbon accumulates on the discharge's tube wall as residue, while the gas/nuclei stream is gradually withdrawn from the hot plasma region in the outlet plasma stream, where 'flowing' graphene sheets are assembled. The diffusion of gas-phase carbon was estimated from detailed analysis of the experimental data. The influence of additional hydrogen in the background gas mixture, i.e. Ar/ C_2H_5OH / H_2 ratio, on the structural quality of fabricated graphene sheets and, in particular, on the sp^3/sp^2 carbon ratio was analyzed. Raman spectroscopy, SEM, and XPS techniques were applied to analyze the changes in graphene sheet composition and structure as a function of the amount of hydrogen in the background

gas mixture. The model predictions were validated by experimental results.

2. Experimental

Flowing graphene sheets were assembled using a microwave plasma sustained by surface waves. A surface-wave-driven plasma is a special type of microwave plasma where the microwave power is transferred to the plasma by the electric field of a guided wave [33]. The scheme of the experimental setup is shown in figure 1. Microwaves at 2.45 GHz were provided by a generator (Sairem) with maximum power of 2 kW. The microwaves traveled through a waveguide system (WR-340), which included a water-cooled circulator, directional couplers, a three-stub tuner, a moveable short-circuit, and a waveguide surfatron as a field applicator. By adjusting the movable short-circuit and the three-stub tuners, optimal impedance matching conditions are set and the coupling of the electric field to the discharge is maximized. The discharge is ignited inside a quartz tube (1.5 cm inner and 1.8 cm outer diameters) placed vertically and perpendicularly to the waveguide's widest wall. The gas mixture is injected into the discharge under laminar flow conditions and consists of premixed Ar (purity of 99.999%) and ethanol vapor.

The ethanol vapor was introduced into the discharge using a bubbling system (see figure 1). For this purpose, the total Ar flux Q_{Ar}^{tot} was divided into two branches, as shown in figure 1: $Q_{Ar}^{tot} = Q_{Ar} + Q_{Ar/Et}$. While the first branch (Q_{Ar}) flowed directly into the discharge, the other branch passed through a tank filled with ethanol ($Q_{Ar/Et}$) in order to drag ethanol molecules. The partial ethanol flow was managed via rigid control of the liquid temperature [28]. Additionally, pure H_2 gas was introduced in the background gas mixture. The partial H_2 flow was changed in the range of 1–2.5 sccm. Hence, the total gas flow introduced into the discharge was $Q^{tot} = Q_{Ar}^{tot} + Q_{Et} + Q_{H_2}$. Externally forced heating in the assembly zone of the plasma reactor using heat exchanger (figure 1) was applied to engineer the structural qualities of the assembled graphene sheets as described in Tatarova *et al* [28].

All carbon nanostructures were synthesized by fixing the wall temperature in the assembly zone at 100°C. The nanostructures were captured by a membrane filter system coupled to an Edwards BS2212 two-stage rotary vacuum pump. All the experiments were performed at the optimal conditions for graphene sheet synthesis, i.e. $Q_{Ar} = 250$ sccm, $Q_{Et} = 0.6$ sccm, and $P = 700$ – 900 W [28].

A photo of the plasma reactor used is shown in figure 2. The incident laser (532 nm) beam is scattered from the flowing graphene sheets and appears as a green broken line on the photo.

To control the output gas products, a part of the outlet gas from the plasma reactor was probed by a Stanford Research System RGA 200 mass analyzer and a Fourier-transform infrared Nicolet 5700 spectrometer in the wave number range 1000–4000 cm^{-1} .

The relative concentrations of C_2 , H_2 and H species in a hot plasma zone were monitored using optical emission

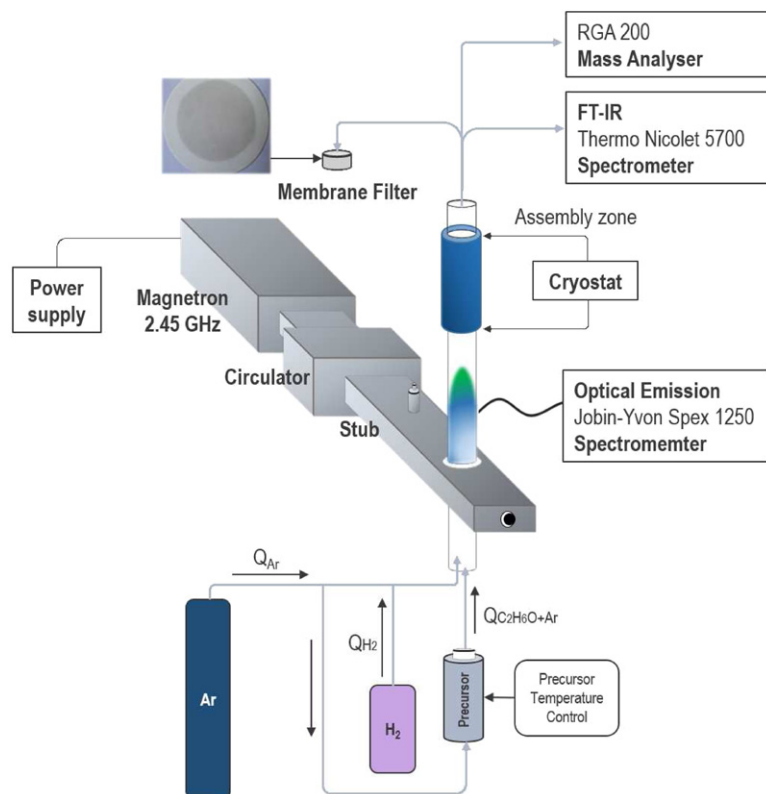


Figure 1. Experimental setup.

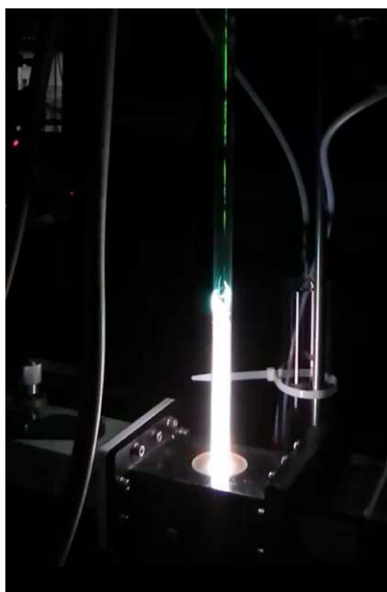


Figure 2. Photo of the plasma column and flowing graphene sheets radiated by a laser beam (stacks.iop.org/PSST/25/015013/mmedia).

spectroscopy. The light emitted by the plasma was collected by an optical fiber and directed to the entrance of a Jobin-Yvon Spex 1250 spectrometer (2400 g mm^{-1} grating) equipped with a charge-coupled device (CCD) camera. The plasma emission in the 300–700 nm range was investigated. Gas temperature in the hot plasma zone was determined using rotational distribution of OH ($A^2\Sigma^+, v = 0 \rightarrow X^2\Pi_i, v' = 0$) band in the 300–315 nm spectral range assuming equilibrium between

rotational and translational degree of freedom [28]. Infrared-sensitive measurement of the wall-temperature axial profile using an optical thermometer was performed.

The obtained solid carbon residue formed at the wall in the assembly zone of plasma reactor was analyzed by SEM. A JEOL, JSM-7001F field emission gun scanning electron microscope operating in secondary electron imaging mode (SEI) with applied voltages in the range of 10–15 kV, while free standing graphene sheets were analyzed by a high-resolution Zeiss Neon 40.

For Raman spectroscopy analysis, the synthesized nanostructures were suspended on a glass substrate, then Raman spectra from different regions on the substrate were obtained using a LabRAM HR Visible (Horiba Jobin-Yvon) Raman spectrometer with 1 cm^{-1} spectral resolution and 633 nm Ne–Ne laser excitation with laser spot size of $2 \mu\text{m}$. Measurements were performed with a laser power $P_1 = 0.054 \text{ mW}$ to avoid overheating.

XPS elemental analysis of the synthesized graphene sheets was performed using a KRATOS XSAM800 x-ray spectrometer with a double anode. The spectrometer was operated in fixed analyzer transmission mode with an analyzer pass energy of 20 eV and nonmonochromatic x-ray source (Mg $K\alpha$ line) with a power of 120 W ($12 \text{ kV} \times 10 \text{ mA}$). Samples were analyzed at room temperature at UHV pressure $\sim 10^{-7} \text{ Pa}$ and the takeoff angle set to 90° . Carbon material was peeled off the filters using the XPS sample holder with double-sided tape. The spectra were collected in 0.1-eV steps using a Sun SPARC Station 4 with Vision software (Kratos). X-ray source satellites were subtracted. Shirley backgrounds and Gaussian/

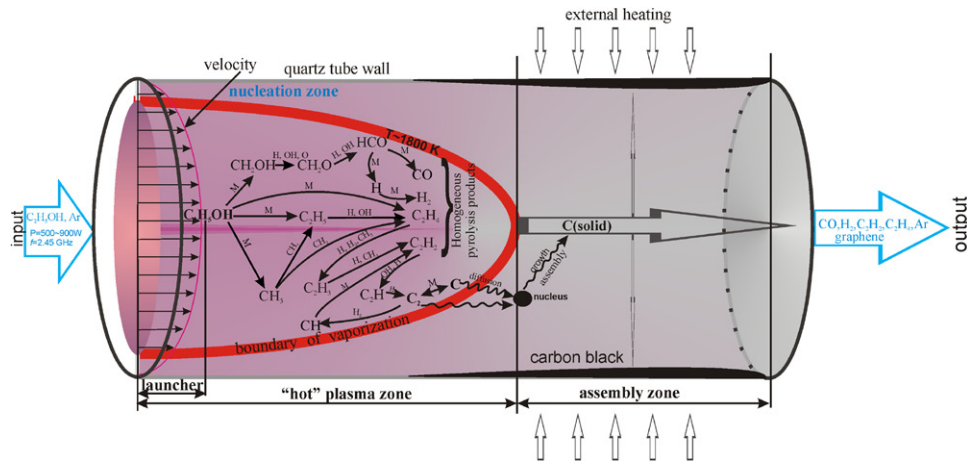


Figure 3. Scheme of the main processes in hot plasma and assembly zones.

Lorentzian line shapes were fitted using XPS Peak 4.1 (free-ware). No flood gun was used for charge compensation.

3. Theoretical model

The plasma reactor was modeled as consisting of different zones as presented in figure 3. The first one, surface wave sustained discharge zone, included the zone inside the launcher and the extended hot plasma zone just beyond the launcher (figure 1). There, the surface wave power was absorbed by plasma electrons, which transfer the energy to heavy particles via elastic and inelastic collisions, so that high gas temperatures (up to 2200 K) are being achieved. The gas temperature in this first zone is nearly constant and then drops sharply in the next zone, the ‘near’ (10–13 cm) afterglow plasma zone [34]. It should be noted that the gas temperature is also radially inhomogeneous, with radial profile close to the parabolic one. Those two regions form the hot plasma zone. The next zone in axial direction that includes the plasma afterglow (~20 cm) is the ‘assembly zone’ (see figures 2 and 3) where kinetic processes of growth and assembly of carbon nanostructures take place.

As already noted, the carbon nucleation process is determined by the interplay of thermodynamic and kinetic factors. For this reason the present model was based on a set of nonlinearly coupled and spatially dependent differential equations describing plasma thermodynamics and chemical kinetics [35]. The input parameters were externally controlled, i.e. gas flows, total power delivered to the launcher, pressure and gas mixture, i.e. Ar/C₂H₅OH/H₂, injected into the discharge. The fluxes of Ar and C₂H₅OH were kept constant ($Q_{Ar} = 250$ sccm, $Q_{Et} = 0.6$ sccm) while the flux of H₂ changed from 1 to 2.5 sccm. It was assumed that the total microwave power delivered to the launcher was linearly dissipated along the generated plasma column.

Under atmospheric pressure conditions the collisions occur frequently enough (for instance the electron-neutral collision frequency is $\sim 10^{11}$ s⁻¹) to compensate to some extent the effect of nonequilibrium factors and local thermal equilibrium can be nearly approached. Hence, local thermal equilibrium

was assumed. Additionally, the experimentally measured wall temperature profile was adopted as a boundary value for the gas temperature. Only axial variations (1D model) of the gas temperature as a key plasma parameter and particle densities were taken into consideration.

A kinetic scheme similar to that presented by Marinov [35] was used. To account for the formation of the solid carbon both in the effluent plasma/gas flows and deposited on the tube walls, detailed kinetics of C₂ radicals and carbon atoms C were considered. Several new chemical reactions for carbonic–dicarbonic submechanisms were added. The present scheme includes 57 components of ethanol fragmentation and ~390 chemical reactions [36–41], which are presented in table 1. The rate constants were extrapolated to the experimentally determined upper limit of the temperature range (2200 K) using a nonlinear extrapolation method presented in [42]. The expressions for the rate constants in the extended temperature range were validated with available in the literature data [36, 37, 42–45]. The thermodynamic data of the processes were taken from thermodynamic databases [35, 36, 46–48].

Taking into account the external cooling of the quartz tube, the gas temperature $T(r)$ had a maximum in the center of the tube and decreased towards the walls. We assumed a parabolic radial profile for the gas temperature, i.e.

$$T(r) = (T_a - T_w) \left(1 - \left(\frac{r}{R} \right)^2 \right) + T_w, \quad (1)$$

where T_a represents the temperature along the central axis, T_w the wall temperature and R the tube radius. It was further assumed that the main thermal losses were due to the radial heat conduction so that they were expressed as

$$\frac{1}{r} \frac{\partial}{\partial r} \left(r \chi(T) \frac{\partial T}{\partial r} \right) \Big|_{r \rightarrow R} \approx -\frac{4}{R^2} \chi(T) (T_a - T_w), \quad (2)$$

where χ represents the argon thermal conductivity. Under the above assumptions, the gas thermal balance equation can be written as [34]

$$\frac{P_0}{k_B} V_0 \frac{1}{T_0} C_p \frac{dT_a}{dz} = -\frac{4\chi(T)}{R^2} (T_a - T_w) + \frac{\delta}{S} \frac{dP}{dz}, \quad (3)$$

Table 1. Reaction mechanisms of ethanol decomposition with corresponding rate coefficients.

List of Species:

Ar, CH₃OH, H₂, H, HO₂, H₂O₂, H₂O, O, OH, O₂, CH₄, CH₃, CH₂, CH, CH₂O, CH₂(s), CH₂CO, HCO, CH₃O, CO₂, CO, HCOH, CH₂OH, HCCO, C₂O, HCCOH, C₂H, C₂H₂, C₂H₄, C₂H₆, C₂H₅, C₂H₃, H₂CCCH, HCOOH, CH₂CHCO, CH₂CHCHO, CH₃CHCO, C₃H₈, C₃H₂, C₃H₆, C₃H₅(a), C₃H₅(p), C₃H₅(s), C₃H₇(i), C₃H₇(n), C₃H₄(p), C₃H₄(a), CHOCHO, CH₃HCO, C₂H₅OH, C₂H₄OH, CH₃CHOH, CH₃CH₂O, CH₂HCO, CH₃CO, C₂, C

N	Reaction	Rate coefficient (s ⁻¹ or cm ³ s ⁻¹ or cm ⁶ s ⁻¹)	Ref.
Hydrogen–Oxygen submechanism			
1	OH + H ₂ ↔ H + H ₂ O	$3.55 \times 10^{-16} \times T^{1.52} \exp(-1736/T)$	[38]
2	H + O ₂ ↔ OH + O	$1.62 \times 10^{-10} \times \exp(-7476/T)$	[37]
3	O + H ₂ ↔ OH + H	$8.40 \times 10^{-20} \times T^{2.67} \exp(-3167/T)$	[38]
4	H + O ₂ (+M) ↔ HO ₂ (+M)	7.51×10^{-11}	[38]
Third-body efficiencies: H ₂ O 0.0, H ₂ 0.0, CH ₄ 10.0, CO ₂ 3.8, CO 1.9			
Rate coefficient for low pressure limit (cm ³ s ⁻¹): $2.89 \times 10^{-29} \times T^{-1.26}$			
5	H + O ₂ (+H ₂) ↔ HO ₂ (+H ₂)	7.51×10^{-11}	[38]
Third-body efficiencies: H ₂ 1.0			
Rate coefficient for low pressure limit (cm ³ s ⁻¹): $4.19 \times 10^{-29} \times T^{-1.13}$			
6	H + O ₂ (+H ₂ O) ↔ HO ₂ (+H ₂ O)	7.51×10^{-11}	[38]
Third-body efficiencies: H ₂ O 1.0			
Rate coefficient for low pressure limit (cm ³ s ⁻¹): $5.79 \times 10^{-25} \times T^{-2.44}$			
7	OH + HO ₂ ↔ H ₂ O + O ₂	$3.54 \times 10^{04} \times T^{-4.83} \exp(1762/T)$	[38]
8	OH + HO ₂ ↔ H ₂ O + O ₂	$1.51 \times 10^{-09} \times \exp(-5520/T)$	[39]
9	H + HO ₂ ↔ OH + OH	$2.49 \times 10^{-10} \times \exp(-503/T)$	[38]
10	H + HO ₂ ↔ H ₂ + O ₂	$1.10 \times 10^{-10} \times \exp(-1070/T)$	[40]
11	H + HO ₂ ↔ O + H ₂ O	$5.00 \times 10^{-11} \times \exp(-866/T)$	[38]
12	O + HO ₂ ↔ O ₂ + OH	5.40×10^{-11}	[38]
13	OH + OH ↔ O + H ₂ O	$5.93 \times 10^{-20} \times T^{2.40} \exp(1063/T)$	[38]
14	H + H + M ↔ H ₂ + M	$2.76 \times 10^{-30} \times T^{-1.00}$	[38]
Third-body efficiencies: H ₂ 0.0, H ₂ O 0.0			
15	H + H + H ₂ ↔ H ₂ + H ₂	$2.54 \times 10^{-31} \times T^{-0.60}$	[38]
16	H + H + H ₂ O ↔ H ₂ + H ₂ O	$1.65 \times 10^{-28} \times T^{-1.25}$	[38]
17	H + OH + M ↔ H ₂ O + M	$6.09 \times 10^{-26} \times T^{-2.00}$	[38]
Third-body efficiencies: H ₂ O 6.4			
18	H + O + M ↔ OH + M	$1.30 \times 10^{-29} \times T^{-1.00}$	[38]
Third-body efficiencies: H ₂ O 6.4			
19	O + O + M ↔ O ₂ + M	$5.21 \times 10^{-35} \times \exp(900/T)$	[38]
20	HO ₂ + HO ₂ ↔ H ₂ O ₂ + O ₂	$6.97 \times 10^{-10} \times \exp(-6032/T)$	[38]
21	HO ₂ + HO ₂ ↔ H ₂ O ₂ + O ₂	$2.16 \times 10^{-13} \times \exp(820/T)$	[38]
22	OH + OH(+M) ↔ H ₂ O ₂ (+M)	$2.06 \times 10^{-10} \times T^{-0.37}$	[38]
Troé parameters: $a = 0.470$, $T^{***} = 100.0$, $T^* = 2000.0$, $T^{**} = 1.0 \times 10^{15}$			
Rate coefficient for low pressure limit (cm ³ s ⁻¹): $8.38 \times 10^{-18} \times T^{-4.63} \times \exp(1032/T)$			
23	H ₂ O ₂ + H ↔ HO ₂ + H ₂	$3.29 \times 10^{-18} \times T^{2.00} \exp(-1226/T)$	[38]
24	H ₂ O ₂ + H ↔ OH + H ₂ O	$5.10 \times 10^{-11} \times \exp(-2123/T)$	[38]
25	H ₂ O ₂ + O ↔ OH + HO ₂	$1.59 \times 10^{-17} \times T^{2.00} \exp(-1999/T)$	[38]
26	H ₂ O ₂ + OH ↔ HO ₂ + H ₂ O	1.66×10^{-12}	[37]
27	H ₂ O ₂ + OH ↔ HO ₂ + H ₂ O	$9.63 \times 10^{-10} \times \exp(-4813/T)$	[37]
C ₁ hydrocarbon submechanism			
28	CH ₃ + CH ₃ (+M) ↔ C ₂ H ₆ (+M)	$1.53 \times 10^{-07} \times T^{-1.17} \times \exp(320/T)$	[39]
Third-body efficiencies: H ₂ O 5.0, H ₂ 2.0, CO ₂ 3.0, CO 2.0			
Troé parameters: $a = 0.405$, $T^{***} = 1120.0$, $T^* = 69.6$, $T^{**} = 10^{15}$			
Rate coefficient for low pressure limit (cm ³ s ⁻¹): $3.14 \times 10^{-12} \times T^{-5.25} \times \exp(858/T)$			
29	CH ₃ + H(+M) ↔ CH ₄ (+M)	$3.55 \times 10^{-9} \times T^{-0.40}$	[39]
Third-body efficiencies: H ₂ O 5.0, H ₂ 2.0, CO ₂ 3.0, CO 2.0			
Troé parameters: $a = 0.0$, $T^{***} = 10^{-15}$, $T^* = 1.0 \times 10^{-15}$, $T^{**} = 40.0$			
Rate coefficient for low pressure limit (cm ³ s ⁻¹): $9.13 \times 10^{-18} \times T^{-4.00} \exp(1061/T)$			
30	CH ₄ + H ↔ CH ₃ + H ₂	$3.65 \times 10^{-20} \times T^{3.00} \exp(-4405/T)$	[39]

Table 1. (Continued.)

N	Reaction	Rate coefficient (s^{-1} or $cm^3 s^{-1}$ or $cm^6 s^{-1}$)	Ref.
31	$CH_4 + OH \leftrightarrow CH_3 + H_2O$	$6.96 \times 10^{-18} \times T^{2.00} \exp(-1282/T)$	[38]
32	$CH_4 + O \leftrightarrow CH_3 + OH$	$1.15 \times 10^{-15} \times T^{1.56} \exp(-4272/T)$	[38]
33	$CH_4 + HO_2 \leftrightarrow CH_3 + H_2O_2$	$1.86 \times 10^{-11} \times \exp(-12405/T)$	[38]
34	$CH_3 + HO_2 \leftrightarrow CH_3O + OH$	1.16×10^{-11}	[35]
35	$CH_3 + HO_2 \leftrightarrow CH_4 + O_2$	4.98×10^{-12}	[38]
36	$CH_3 + O \leftrightarrow CH_2O + H$	1.33×10^{-10}	[38]
37	$CH_3 + O_2 \leftrightarrow CH_3O + O$	$2.41 \times 10^{-11} \times \exp(-14705/T)$	[35]
38	$CH_3 + O_2 \leftrightarrow CH_2O + OH$	$4.17 \times 10^{-13} \times \exp(-7370/T)$	[38]
39	$CH_3O + H \leftrightarrow CH_3 + OH$	1.66×10^{-11}	[39]
40	$CH_2OH + H \leftrightarrow CH_3 + OH$	1.66×10^{-11}	[39]
41	$CH_3 + OH \leftrightarrow CH_2(s) + H_2O$	$3.32 \times 10^{-11} \times \exp(-277/T)$	[35]
42	$CH_3 + OH \leftrightarrow HCOH + H_2$	$1.66 \times 10^{-14} \times \exp(209/T)$	[35]
43	$CH_3 + OH \leftrightarrow CH_2 + H_2O$	$4.98 \times 10^{-18} \times T^{2.00} \exp(-1259/T)$	[39]
44	$CH_3 + H \leftrightarrow CH_2 + H_2$	$1.49 \times 10^{-10} \times \exp(-7602/T)$	[35]
45	$CH_3 + M \leftrightarrow CH + H_2 + M$	$1.15 \times 10^{-9} \times \exp(-41518/T)$	[35]
46	$CH_3 + M \leftrightarrow CH_2 + H + M$	$3.16 \times 10^{-8} \times \exp(-46020/T)$	[35]
47	$CH_3 + OH(+M) \leftrightarrow CH_3OH(+M)$	$1.44 \times 10^{-10} \times T^{0.10}$	[35]
Third-body efficiencies: H_2O 10.0, H_2 2.0, CO_2 3.0, CO 2.0			
Troé parameters: $a = 0.025$, $T^{***} = 10^{-15}$, $T^* = 8000.0$, $T^{**} = 3000.0$			
Rate coefficient for low pressure limit ($cm^3 s^{-1}$): $2.44 \times 10^{-06} \times T^{-7.40} \exp(315/T)$			
48	$CH_3OH(+M) \leftrightarrow CH_2(s) + H_2O(+M)$	$2.84 \times 10^{10} \times T \times \exp(-42224/T)$	[35]
Third-body efficiencies H_2O 10.0, H_2 2.0, CO_2 3.0, CO 2.0			
Troé parameters: $a = 0.9$, $T^{***} = 740.0$, $T^* = 980.0$, $T^{**} = 5100$			
Rate coefficient for low pressure limit ($cm^3 s^{-1}$): $2.96 \times 10^{25} \times T^{-8.81} \exp(47005/T)$			
49	$CH_3OH(+M) \leftrightarrow HCOH + H_2(+M)$	$4.20 \times 10^{09} \times T^{1.12} \exp(-43096/T)$	[35]
Third-body efficiencies: H_2O 10.0, H_2 2.0, CO_2 3.0, CO 2.0			
Troé parameters: $a = 0.9$, $T^{***} = 615.0$, $T^* = 915.0$, $T^{**} = 4615.0$			
Rate coefficient for low pressure limit ($cm^3 s^{-1}$): $8.34 \times 10^{23} \times T^{-8.40} \exp(47737/T)$			
50	$CH_3OH(+M) \leftrightarrow CH_2O + H_2(+M)$	$2.03 \times 10^{09} \times T \times \exp(-46036/T)$	[35]
Third-body efficiencies: H_2O 10.0, H_2 2.0, CO_2 3.0, CO 2.0			
Troé parameters: $a = 0.9$, $T^{***} = 825.0$, $T^* = 1125.0$, $T^{**} = 5700.0$			
Rate coefficient for low pressure limit ($cm^3 s^{-1}$): $1.63 \times 10^{24} \times T^{-8.40} \times \exp(51230/T)$			
51	$CH_3OH + OH \leftrightarrow CH_2OH + H_2O$	$4.33 \times 10^{-19} \times T^{2.18} \times \exp(677/T)$	[35]
52	$CH_3OH + OH \leftrightarrow CH_3O + H_2O$	$4.35 \times 10^{-18} \times T^{2.06} \times \exp(-461/T)$	[40]
53	$CH_3OH + O \leftrightarrow CH_2OH + OH$	$6.44 \times 10^{-19} \times T^{2.50} \exp(-1551/T)$	[40]
54	$CH_3OH + H \leftrightarrow CH_2OH + H_2$	$2.82 \times 10^{-17} \times T^{2.10} \exp(-2451/T)$	[40]
55	$CH_3OH + H \leftrightarrow CH_3O + H_2$	$7.04 \times 10^{-18} \times T^{2.10} \exp(-2451/T)$	[40]
56	$CH_3OH + CH_3 \leftrightarrow CH_2OH + CH_4$	$5.30 \times 10^{-23} \times T^{3.17} \exp(-3610/T)$	[40]
57	$CH_3OH + CH_3 \leftrightarrow CH_3O + CH_4$	$2.41 \times 10^{-23} \times T^{3.10} \exp(-3491/T)$	[40]
58	$CH_3OH + HO_2 \leftrightarrow CH_2OH + H_2O_2$	$1.60 \times 10^{-13} \times \exp(-6332/T)$	[40]
59	$CH_2O + H(+M) \leftrightarrow CH_3O(+M)$	$8.97 \times 10^{-13} \times T^{0.45} \exp(-1309/T)$	[36]
Third-body efficiencies: H_2O 5.0			
Troé parameters: $a = 0.758$, $T^{***} = 94.0$, $T^* = 1555.0$, $T^{**} = 4200.0$			
Rate coefficient for low pressure limit ($cm^3 s^{-1}$): $4.14 \times 10^{-18} \times T^{-4.80} \times \exp(2799/T)$			
60	$CH_2O + H(+M) \leftrightarrow CH_2OH(+M)$	$8.97 \times 10^{-13} \times T^{0.45} \times \exp(-1812/T)$	[36]
Third-body efficiencies: H_2O 5.0			
Troé parameters: $a = 0.7187$, $T^{***} = 103.0$, $T^* = 1291.0$, $T^{**} = 4160$.			
Rate coefficient for low pressure limit ($cm^3 s^{-1}$): $2.51 \times 10^{-16} \times T^{-4.82} \times \exp(3287/T)$			
61	$CH_3O + CH_3 \leftrightarrow CH_2O + CH_4$	1.99×10^{-11}	[36]
62	$CH_3O + H \leftrightarrow CH_2O + H_2$	3.32×10^{-11}	[36]
63	$CH_2OH + H \leftrightarrow CH_2O + H_2$	3.32×10^{-11}	[35]
64	$CH_3O + OH \leftrightarrow CH_2O + H_2O$	1.66×10^{-11}	[35]
65	$CH_2OH + OH \leftrightarrow CH_2O + H_2O$	1.66×10^{-11}	[35]

(Continued)

Table 1. (Continued.)

N	Reaction	Rate coefficient (s^{-1} or $\text{cm}^3 \text{s}^{-1}$ or $\text{cm}^6 \text{s}^{-1}$)	Ref.
66	$\text{CH}_3\text{O} + \text{O} \leftrightarrow \text{CH}_2\text{O} + \text{OH}$	1.66×10^{-11}	[35]
67	$\text{CH}_2\text{OH} + \text{O} \leftrightarrow \text{CH}_2\text{O} + \text{OH}$	1.66×10^{-11}	[35]
68	$\text{CH}_3\text{O} + \text{O}_2 \leftrightarrow \text{CH}_2\text{O} + \text{HO}_2$	$1.05 \times 10^{-13} \times \exp(-1309/T)$	[35]
69	$\text{CH}_3\text{O} + \text{CO} \leftrightarrow \text{CH}_3 + \text{CO}_2$	$7.77 \times 10^{-22} \times T^{3.16} \exp(-2708/T)$	[35]
70	$\text{CH}_2\text{OH} + \text{O}_2 \leftrightarrow \text{CH}_2\text{O} + \text{HO}_2$	$2.61 \times 10^{-09} \times T^{-1.00}$	[35]
71	$\text{CH}_2\text{OH} + \text{O}_2 \leftrightarrow \text{CH}_2\text{O} + \text{HO}_2$	$1.20 \times 10^{-10} \times \exp(-1801/T)$	[35]
72	$\text{HCOH} + \text{OH} \leftrightarrow \text{HCO} + \text{H}_2\text{O}$	3.32×10^{-11}	[39]
73	$\text{HCOH} + \text{H} \leftrightarrow \text{CH}_2\text{O} + \text{H}$	3.32×10^{-10}	[39]
74	$\text{HCOH} + \text{O} \rightarrow \text{CO} + \text{OH} + \text{H}$	1.33×10^{-10}	[39]
75	$\text{HCOH} + \text{O}_2 \rightarrow \text{CO} + \text{OH} + \text{OH}$	1.66×10^{-11}	[39]
76	$\text{HCOH} + \text{O}_2 \leftrightarrow \text{CO}_2 + \text{H}_2\text{O}$	1.66×10^{-11}	[39]
77	$\text{HCOH} \leftrightarrow \text{CH}_2\text{O}$	$2.10 \times 10^{19} \times T^{-3.07} \exp(15959/T)$	[39]
78	$\text{CH} + \text{H}_2 \leftrightarrow \text{H} + \text{CH}_2$	$1.79 \times 10^{-10} \times \exp(-1566/T)$	[36]
79	$\text{CH}_2 + \text{OH} \leftrightarrow \text{CH} + \text{H}_2\text{O}$	$1.88 \times 10^{-17} \times T^{2.00} \exp(-1510/T)$	[35]
80	$\text{CH}_2 + \text{OH} \leftrightarrow \text{CH}_2\text{O} + \text{H}$	4.15×10^{-11}	[35]
81	$\text{CH}_2 + \text{CO}_2 \leftrightarrow \text{CH}_2\text{O} + \text{CO}$	$1.83 \times 10^{-13} \times \exp(-503/T)$	[35]
82	$\text{CH}_2 + \text{O} \rightarrow \text{CO} + \text{H} + \text{H}$	8.30×10^{-11}	[35]
83	$\text{CH}_2 + \text{O} \leftrightarrow \text{CO} + \text{H}_2$	4.98×10^{-11}	[35]
84	$\text{CH}_2 + \text{O}_2 \leftrightarrow \text{CH}_2\text{O} + \text{O}$	$5.46 \times 10^{-03} \times T^{-3.30} \exp(1444/T)$	[39]
85	$\text{CH}_2 + \text{O}_2 \rightarrow \text{CO}_2 + \text{H} + \text{H}$	$5.46 \times 10^{-03} \times T^{-3.30} \exp(1444/T)$	[39]
86	$\text{CH}_2 + \text{O}_2 \leftrightarrow \text{CO}_2 + \text{H}_2$	$1.68 \times 10^{-03} \times T^{-3.30} \exp(759/T)$	[39]
87	$\text{CH}_2 + \text{O}_2 \leftrightarrow \text{CO} + \text{H}_2\text{O}$	$1.21 \times 10^{-04} \times T^{-2.54} \exp(911/T)$	[39]
88	$\text{CH}_2 + \text{O}_2 \leftrightarrow \text{HCO} + \text{OH}$	$2.14 \times 10^{-04} \times T^{-3.30} \exp(143/T)$	[39]
89	$\text{CH}_2 + \text{CH}_3 \leftrightarrow \text{C}_2\text{H}_4 + \text{H}$	6.64×10^{-11}	[35]
90	$\text{CH}_2 + \text{HCCO} \leftrightarrow \text{C}_2\text{H}_3 + \text{CO}$	4.98×10^{-11}	[35]
91	$\text{CH}_2(\text{s}) + \text{M} \leftrightarrow \text{CH}_2 + \text{M}$	$1.49 \times 10^{-11} \times \exp(-302/T)$	[36]
Third body efficiencies: H 12.0, H ₂ O 3.0, C ₂ H ₂ 4.0			
92	$\text{CH}_2(\text{s}) + \text{CH}_4 \leftrightarrow \text{CH}_3 + \text{CH}_3$	6.64×10^{-11}	[35]
93	$\text{CH}_2(\text{s}) + \text{C}_2\text{H}_6 \leftrightarrow \text{CH}_3 + \text{C}_2\text{H}_5$	1.99×10^{-10}	[35]
94	$\text{CH}_2(\text{s}) + \text{O}_2 \rightarrow \text{CO} + \text{OH} + \text{H}$	1.16×10^{-10}	[35]
95	$\text{CH}_2(\text{s}) + \text{H}_2 \leftrightarrow \text{CH}_3 + \text{H}$	1.16×10^{-10}	[35]
96	$\text{CH}_2(\text{s}) + \text{C}_2\text{H}_4 \leftrightarrow \text{C}_3\text{H}_5(\text{a}) + \text{H}$	2.16×10^{-10}	[35]
97	$\text{CH}_2(\text{s}) + \text{O} \rightarrow \text{CO} + \text{H} + \text{H}$	4.98×10^{-11}	[35]
98	$\text{CH}_2(\text{s}) + \text{OH} \leftrightarrow \text{CH}_2\text{O} + \text{H}$	4.98×10^{-11}	[35]
99	$\text{CH}_2(\text{s}) + \text{H} \leftrightarrow \text{CH} + \text{H}_2$	4.98×10^{-11}	[35]
100	$\text{CH}_2(\text{s}) + \text{CO}_2 \leftrightarrow \text{CH}_2\text{O} + \text{CO}$	4.98×10^{-12}	[35]
101	$\text{CH}_2(\text{s}) + \text{CH}_3 \leftrightarrow \text{C}_2\text{H}_4 + \text{H}$	3.32×10^{-11}	[35]
102	$\text{CH}_2(\text{s}) + \text{CH}_2\text{CO} \leftrightarrow \text{C}_2\text{H}_4 + \text{CO}$	2.66×10^{-10}	[35]
103	$\text{CH} + \text{O}_2 \leftrightarrow \text{HCO} + \text{O}$	5.48×10^{-11}	[35]
104	$\text{CH} + \text{O} \leftrightarrow \text{CO} + \text{H}$	9.47×10^{-11}	[35]
105	$\text{CH} + \text{OH} \leftrightarrow \text{HCO} + \text{H}$	4.98×10^{-11}	[35]
106	$\text{CH} + \text{CO}_2 \leftrightarrow \text{HCO} + \text{CO}$	$5.65 \times 10^{-12} \times \exp(-347/T)$	[35]
107	$\text{CH} + \text{H}_2\text{O} \leftrightarrow \text{CH}_2\text{O} + \text{H}$	$1.94 \times 10^{-09} \times T^{-0.75}$	[35]
108	$\text{CH} + \text{CH}_2\text{O} \leftrightarrow \text{CH}_2\text{CO} + \text{H}$	$1.57 \times 10^{-10} \times \exp(259/T)$	[35]
109	$\text{CH} + \text{CH}_3 \leftrightarrow \text{C}_2\text{H}_3 + \text{H}$	4.98×10^{-11}	[35]
110	$\text{CH} + \text{CH}_4 \leftrightarrow \text{C}_2\text{H}_4 + \text{H}$	9.96×10^{-11}	[35]
111	$\text{HCOOH} + \text{M} \leftrightarrow \text{CO} + \text{H}_2\text{O} + \text{M}$	$3.47 \times 10^{-10} \times \exp(-20339/T)$	[35]
112	$\text{HCOOH} + \text{M} \leftrightarrow \text{CO}_2 + \text{H}_2 + \text{M}$	$2.24 \times 10^{-09} \times \exp(-30508/T)$	[35]
113	$\text{HCOOH} + \text{OH} \rightarrow \text{CO}_2 + \text{H}_2\text{O} + \text{H}$	$4.35 \times 10^{-18} \times T^{2.06} \exp(-461/T)$	[35]
114	$\text{HCOOH} + \text{OH} \rightarrow \text{CO} + \text{H}_2\text{O} + \text{OH}$	$3.07 \times 10^{-17} \times T^{1.50} \exp(484/T)$	[39]
115	$\text{HCOOH} + \text{H} \rightarrow \text{CO}_2 + \text{H}_2 + \text{H}$	$7.04 \times 10^{-18} \times T^{2.10} \exp(-2451/T)$	[39]
116	$\text{HCOOH} + \text{H} \rightarrow \text{CO} + \text{H}_2 + \text{OH}$	$1.01 \times 10^{-10} \times T^{-0.35} \exp(1504/T)$	[39]
117	$\text{HCOOH} + \text{CH}_3 \rightarrow \text{CH}_4 + \text{CO} + \text{OH}$	$6.48 \times 10^{-31} \times T^{5.80} \exp(-1108/T)$	[39]

Table 1. (Continued.)

N	Reaction	Rate coefficient (s^{-1} or $cm^3 s^{-1}$ or $cm^6 s^{-1}$)	Ref.
118	$HCOOH + HO_2 \rightarrow CO + H_2O_2 + OH$	$3.98 \times 10^{-05} \times T^{-2.20} \exp(7063/T)$	[39]
119	$HCOOH + O \rightarrow CO + OH + OH$	$2.94 \times 10^{-06} \times T^{-1.90} \exp(1498/T)$	[39]
120	$CH_2O + OH \leftrightarrow HCO + H_2O$	$5.70 \times 10^{-15} \times T^{1.18} \exp(225/T)$	[40]
121	$CH_2O + H \leftrightarrow HCO + H_2$	$3.64 \times 10^{-16} \times T^{1.77} \exp(-1510/T)$	[35]
122	$CH_2O + M \leftrightarrow HCO + H + M$	$5.50 \times 10^{-08} \times \exp(-40778/T)$	[35]
123	$CH_2O + O \leftrightarrow HCO + OH$	$2.99 \times 10^{-11} \times \exp(-1551/T)$	[35]
124	$HCO + O_2 \leftrightarrow CO + HO_2$	$1.26 \times 10^{-11} \times \exp(-206/T)$	[35]
125	$HCO + M \leftrightarrow H + CO + M$	$3.09 \times 10^{-07} \times T^{-1.00} \exp(8558/T)$	[35]
Third-body efficiencies: H_2 1.87, H_2O 5.0, CH_4 2.81, CO_2 3.0, CO 1.87			
126	$HCO + OH \leftrightarrow H_2O + CO$	1.66×10^{-10}	[35]
127	$HCO + H \leftrightarrow CO + H_2$	$1.98 \times 10^{-11} \times T^{0.25}$	[35]
128	$HCO + O \leftrightarrow CO + OH$	4.98×10^{-11}	[35]
129	$HCO + O \leftrightarrow CO_2 + H$	4.98×10^{-11}	[35]
130	$CO + OH \leftrightarrow CO_2 + H$	$1.56 \times 10^{-20} \times T^{2.25} \exp(1184/T)$	[39]
131	$CO + O + M \leftrightarrow CO_2 + M$	$1.70 \times 10^{-33} \times \exp(-1510/T)$	[35]
132	$CO + O_2 \leftrightarrow CO_2 + O$	$4.20 \times 10^{-12} \times \exp(-24008/T)$	[35]
133	$CO + HO_2 \leftrightarrow CO_2 + OH$	$9.63 \times 10^{-11} \times \exp(-11546/T)$	[35]
C₂ HYDROCARBON SUBMECHANISM			
134	$C_2H_5OH(+M) \leftrightarrow CH_3 + CH_2OH(+M)$	$5.94 \times 10^{23} \times T^{-1.68} \exp(45895/T)$	[39]
Third-body efficiencies: H_2O 5.0, H_2 2.0, CO_2 3.0, CO 2.0			
Trope parameters: $a = 0.5$, $T^{***} = 200.0$, $T^* = 890.0$, $T^{**} = 4600.0$			
Rate coefficient for low pressure limit ($cm^3 s^{-1}$): $4.78 \times 10^{61} \times T^{-18.90} \exp(55335/T)$			
135	$C_2H_5OH(+M) \leftrightarrow C_2H_5 + OH(+M)$	$1.25 \times 10^{23} \times T^{-1.54} \exp(48332/T)$	[39]
Third-body efficiencies: H_2O 5.0, H_2 2.0, CO_2 3.0, CO 2.0			
Trope parameters: $a = 0.5$, $T^{***} = 300.0$, $T^* = 900.0$, $T^{**} = 5000.0$			
Rate coefficient for low pressure limit ($cm^3 s^{-1}$): $5.40 \times 10^{61} \times T^{-18.81} \times \exp(57860/T)$			
136	$C_2H_5OH(+M) \leftrightarrow C_2H_4 + H_2O(+M)$	$2.79 \times 10^{13} \times T^{0.09} \exp(-33295/T)$	[39]
Third-body efficiencies: H_2O 5.0, H_2 2.0, CO_2 3.0, CO 2.0			
Trope parameters: $a = 0.70$, $T^{***} = 350.0$, $T^* = 800.0$, $T^{**} = 3800.0$			
Rate coefficient for low pressure limit ($cm^3 s^{-1}$): $4.27 \times 10^{59} \times T^{-18.85} \exp(43523/T)$			
137	$C_2H_5OH(+M) \leftrightarrow CH_3HCO + H_2(+M)$	$7.24 \times 10^{11} \times T^{0.10} \exp(-45816/T)$	[39]
Third-body efficiencies: H_2O 5.0, H_2 2.0, CO_2 3.0, CO 2.0			
Trope parameters: $a = 0.9$, $T^{***} = 900.0$, $T^* = 1100.0$, $T^{**} = 3500.0$			
Rate coefficient for low pressure limit ($cm^3 s^{-1}$): $7.41 \times 10^{63} \times T^{-19.42} \exp(58190/T)$			
138	$C_2H_5OH + OH \leftrightarrow C_2H_4OH + H_2O$	$2.89 \times 10^{-13} \times T^{0.27} \exp(-302/T)$	[39]
139	$C_2H_5OH + OH \leftrightarrow CH_3CHOH + H_2O$	$7.70 \times 10^{-13} \times T^{0.15}$	[39]
140	$C_2H_5OH + OH \leftrightarrow CH_3CH_2O + H_2O$	$1.24 \times 10^{-12} \times T^{0.30} \exp(-823/T)$	[39]
141	$C_2H_5OH + H \leftrightarrow C_2H_4OH + H_2$	$2.04 \times 10^{-17} \times T^{1.80} \exp(-2567/T)$	[39]
142	$C_2H_5OH + H \leftrightarrow CH_3CHOH + H_2$	$4.28 \times 10^{-17} \times T^{1.65} \exp(-1423/T)$	[39]
143	$C_2H_5OH + H \leftrightarrow CH_3CH_2O + H_2$	$2.49 \times 10^{-17} \times T^{1.60} \exp(-1529/T)$	[39]
144	$C_2H_5OH + O \leftrightarrow C_2H_4OH + OH$	$1.56 \times 10^{-16} \times T^{1.70} \times \exp(-2748/T)$	[39]
145	$C_2H_5OH + O \leftrightarrow CH_3CHOH + OH$	$3.12 \times 10^{-17} \times T^{1.85} \times \exp(-918/T)$	[39]
146	$C_2H_5OH + O \leftrightarrow CH_3CH_2O + OH$	$2.62 \times 10^{-17} \times T^{2.00} \times \exp(-2239/T)$	[39]
147	$C_2H_5OH + CH_3 \leftrightarrow C_2H_4OH + CH_4$	$3.64 \times 10^{-22} \times T^{3.18} \exp(-4844/T)$	[39]
148	$C_2H_5OH + CH_3 \leftrightarrow CH_3CHOH + CH_4$	$1.21 \times 10^{-21} \times T^{2.99} \exp(-4001/T)$	[39]
149	$C_2H_5OH + CH_3 \leftrightarrow CH_3CH_2O + CH_4$	$2.41 \times 10^{-22} \times T^{2.99} \exp(-3851/T)$	[39]
150	$C_2H_5OH + HO_2 \leftrightarrow CH_3CHOH + H_2O_2$	$1.36 \times 10^{-20} \times T^{2.55} \exp(-5412/T)$	[39]
151	$C_2H_5OH + HO_2 \leftrightarrow C_2H_4OH + H_2O_2$	$2.04 \times 10^{-20} \times T^{2.55} \exp(-7929/T)$	[39]
152	$C_2H_5OH + HO_2 \leftrightarrow CH_3CH_2O + H_2O_2$	$4.15 \times 10^{-12} \times \exp(-12082/T)$	[39]
153	$CH_3CH_2O + M \leftrightarrow CH_3HCO + H + M$	$1.93 \times 10^{11} \times T^{-5.89} \exp(12724/T)$	[39]
154	$CH_3CH_2O + M \leftrightarrow CH_3 + CH_2O + M$	$2.24 \times 10^{14} \times T^{-6.96} \exp(11982/T)$	[39]
155	$CH_3CH_2O + O_2 \leftrightarrow CH_3HCO + HO_2$	$6.64 \times 10^{-14} \times \exp(-554/T)$	[39]
156	$CH_3CH_2O + CO \leftrightarrow C_2H_5 + CO_2$	$7.77 \times 10^{-22} \times T^{3.16} \exp(-2708/T)$	[39]

(Continued)

Table 1. (Continued.)

N	Reaction	Rate coefficient (s^{-1} or $\text{cm}^3 \text{s}^{-1}$ or $\text{cm}^6 \text{s}^{-1}$)	Ref.
157	$\text{CH}_3\text{CH}_2\text{O} + \text{H} \leftrightarrow \text{CH}_3 + \text{CH}_2\text{OH}$	4.98×10^{-11}	[39]
158	$\text{CH}_3\text{CH}_2\text{O} + \text{H} \leftrightarrow \text{C}_2\text{H}_4 + \text{H}_2\text{O}$	4.98×10^{-11}	[39]
159	$\text{CH}_3\text{CH}_2\text{O} + \text{OH} \leftrightarrow \text{CH}_3\text{HCO} + \text{H}_2\text{O}$	1.66×10^{-11}	[39]
160	$\text{CH}_3\text{CHOH} + \text{O}_2 \leftrightarrow \text{CH}_3\text{HCO} + \text{HO}_2$	$8.00 \times 10^{-10} \times \exp(-2526/T)$	[39]
161	$\text{CH}_3\text{CHOH} + \text{O}_2 \leftrightarrow \text{CH}_3\text{HCO} + \text{HO}_2$	$1.40 \times 10^{-08} \times T^{-1.20}$	[39]
162	$\text{CH}_3\text{CHOH} + \text{CH}_3 \leftrightarrow \text{C}_3\text{H}_6 + \text{H}_2\text{O}$	1.66×10^{-11}	[39]
163	$\text{CH}_3\text{CHOH} + \text{O} \leftrightarrow \text{CH}_3\text{HCO} + \text{OH}$	1.66×10^{-10}	[39]
164	$\text{CH}_3\text{CHOH} + \text{H} \leftrightarrow \text{C}_2\text{H}_4 + \text{H}_2\text{O}$	4.98×10^{-11}	[39]
165	$\text{CH}_3\text{CHOH} + \text{H} \leftrightarrow \text{CH}_3 + \text{CH}_2\text{OH}$	4.98×10^{-11}	[39]
166	$\text{CH}_3\text{CHOH} + \text{HO}_2 \rightarrow \text{CH}_3\text{HCO} + \text{OH} + \text{OH}$	6.64×10^{-11}	[39]
167	$\text{CH}_3\text{CHOH} + \text{OH} \leftrightarrow \text{CH}_3\text{HCO} + \text{H}_2\text{O}$	8.30×10^{-12}	[39]
168	$\text{CH}_3\text{CHOH} + \text{M} \leftrightarrow \text{CH}_3\text{HCO} + \text{H} + \text{M}$	$1.66 \times 10^{-10} \times \exp(-12586/T)$	[39]
169	$\text{CH}_3\text{HCO} + \text{OH} \leftrightarrow \text{CH}_3\text{CO} + \text{H}_2\text{O}$	$1.53 \times 10^{-17} \times T^{1.50} \exp(484/T)$	[39]
170	$\text{CH}_3\text{HCO} + \text{OH} \leftrightarrow \text{CH}_2\text{HCO} + \text{H}_2\text{O}$	$2.86 \times 10^{-19} \times T^{2.40} \exp(-410/T)$	[35]
171	$\text{CH}_3\text{HCO} + \text{OH} \leftrightarrow \text{CH}_3 + \text{HCOOH}$	$4.98 \times 10^{-09} \times T^{-1.08}$	[39]
172	$\text{CH}_3\text{HCO} + \text{O} \leftrightarrow \text{CH}_3\text{CO} + \text{OH}$	$2.94 \times 10^{-06} \times T^{-1.90} \exp(1498/T)$	[39]
173	$\text{CH}_3\text{HCO} + \text{O} \leftrightarrow \text{CH}_2\text{HCO} + \text{OH}$	$6.18 \times 10^{-11} \times T^{-0.20} \exp(1790/T)$	[39]
174	$\text{CH}_3\text{HCO} + \text{H} \leftrightarrow \text{CH}_3\text{CO} + \text{H}_2$	$7.74 \times 10^{-11} \times T^{-0.35} \exp(1504/T)$	[39]
175	$\text{CH}_3\text{HCO} + \text{H} \leftrightarrow \text{CH}_2\text{HCO} + \text{H}_2$	$3.07 \times 10^{-12} \times T^{0.40} \exp(-2698/T)$	[39]
176	$\text{CH}_3\text{HCO} + \text{CH}_3 \leftrightarrow \text{CH}_3\text{CO} + \text{CH}_4$	$6.48 \times 10^{-31} \times T^{5.80} \exp(-1108/T)$	[39]
177	$\text{CH}_3\text{HCO} + \text{CH}_3 \leftrightarrow \text{CH}_2\text{HCO} + \text{CH}_4$	$4.07 \times 10^{-23} \times T^{3.15} \exp(-2883/T)$	[39]
178	$\text{CH}_3\text{HCO} + \text{HO}_2 \leftrightarrow \text{CH}_3\text{CO} + \text{H}_2\text{O}_2$	$3.98 \times 10^{-05} \times T^{-2.20} \exp(7063/T)$	[39]
179	$\text{CH}_3\text{HCO} + \text{HO}_2 \leftrightarrow \text{CH}_2\text{HCO} + \text{H}_2\text{O}_2$	$3.85 \times 10^{-13} \times T^{0.40} \exp(-7483/T)$	[39]
180	$\text{CH}_3\text{HCO} + \text{O}_2 \leftrightarrow \text{CH}_3\text{CO} + \text{HO}_2$	$1.66 \times 10^{-10} \times \exp(-21245/T)$	[35]
181	$\text{C}_2\text{H}_6 + \text{CH}_3 \leftrightarrow \text{C}_2\text{H}_5 + \text{CH}_4$	$9.13 \times 10^{-25} \times T^{4.00} \exp(-4179/T)$	[35]
182	$\text{C}_2\text{H}_6 + \text{H} \leftrightarrow \text{C}_2\text{H}_5 + \text{H}_2$	$1.91 \times 10^{-16} \times T^{1.90} \exp(-3791/T)$	[28]
183	$\text{C}_2\text{H}_6 + \text{O} \leftrightarrow \text{C}_2\text{H}_5 + \text{OH}$	$4.98 \times 10^{-17} \times T^{2.00} \exp(-2575/T)$	[35]
184	$\text{C}_2\text{H}_6 + \text{OH} \leftrightarrow \text{C}_2\text{H}_5 + \text{H}_2\text{O}$	$1.20 \times 10^{-17} \times T^{2.00} \exp(-435/T)$	[35]
185	$\text{C}_2\text{H}_5 + \text{H} \leftrightarrow \text{C}_2\text{H}_4 + \text{H}_2$	$2.08 \times 10^{-10} \times \exp(-4027/T)$	[38]
186	$\text{C}_2\text{H}_5 + \text{H} \leftrightarrow \text{CH}_3 + \text{CH}_3$	4.98×10^{-11}	[35]
187	$\text{C}_2\text{H}_5 + \text{H} \leftrightarrow \text{C}_2\text{H}_6$	4.98×10^{-11}	[39]
188	$\text{C}_2\text{H}_5 + \text{OH} \leftrightarrow \text{C}_2\text{H}_4 + \text{H}_2\text{O}$	6.64×10^{-11}	[38]
189	$\text{C}_2\text{H}_5 + \text{O} \leftrightarrow \text{CH}_3 + \text{CH}_2\text{O}$	1.66×10^{-10}	[35]
190	$\text{C}_2\text{H}_5 + \text{HO}_2 \leftrightarrow \text{C}_2\text{H}_6 + \text{O}_2$	4.98×10^{-12}	[39]
191	$\text{C}_2\text{H}_5 + \text{HO}_2 \leftrightarrow \text{CH}_3\text{CH}_2\text{O} + \text{OH}$	4.98×10^{-11}	[40]
192	$\text{C}_2\text{H}_5 + \text{O}_2 \leftrightarrow \text{C}_2\text{H}_4 + \text{HO}_2$	$4.80 \times 10^{04} \times T^{-5.40} \exp(3819/T)$	[39]
193	$\text{C}_2\text{H}_5 + \text{O}_2 \leftrightarrow \text{CH}_3\text{HCO} + \text{OH}$	$8.14 \times 10^{-13} \times T^{-0.48} \exp(4207/T)$	[39]
194	$\text{C}_2\text{H}_4 + \text{OH}(+\text{M}) \leftrightarrow \text{C}_2\text{H}_4\text{OH}(+\text{M})$	$3.98 \times 10^{-06} \times T^{-2.30}$	[38]
Third-body efficiencies: H_2O 5.0, H_2 2.0, CO_2 3.0, CO 2.0			
Rate coefficient for low pressure limit ($\text{cm}^3 \text{s}^{-1}$): $4.68 \times 10^{-20} \times T^{-3.50}$			
195	$\text{C}_2\text{H}_4 + \text{OH} \leftrightarrow \text{C}_2\text{H}_3 + \text{H}_2\text{O}$	$3.35 \times 10^{-11} \times \exp(-2988/T)$	[38]
196	$\text{C}_2\text{H}_4 + \text{O} \leftrightarrow \text{CH}_3 + \text{HCO}$	$1.69 \times 10^{-17} \times T^{1.88} \times \exp(-90/T)$	[35]
197	$\text{C}_2\text{H}_4 + \text{O} \leftrightarrow \text{CH}_2\text{HCO} + \text{H}$	$5.63 \times 10^{-18} \times T^{1.88} \exp(-90/T)$	[35]
198	$\text{C}_2\text{H}_4 + \text{CH}_3 \leftrightarrow \text{C}_2\text{H}_3 + \text{CH}_4$	$1.10 \times 10^{-23} \times T^{3.70} \exp(-4783/T)$	[38]
199	$\text{H} + \text{C}_2\text{H}_4 \leftrightarrow \text{C}_2\text{H}_3 + \text{H}_2$	$2.20 \times 10^{-18} \times T^{2.53} \exp(-6162/T)$	[36]
200	$\text{H} + \text{C}_2\text{H}_4(+\text{M}) \leftrightarrow \text{C}_2\text{H}_5(+\text{M})$	$8.97 \times 10^{-13} \times T^{0.45} \times \exp(-916/T)$	[36]
Third-body efficiencies: H_2O 5.0, H_2 2.0, CO_2 3.0, CO 2.0			
Troe parameters: $a = 0.9753$, $T^{***} = 210.00$, $T^* = 984.00$, $T^{**} = 4374.00$			
Rate coefficient for low pressure limit ($\text{cm}^3 \text{s}^{-1}$): $1.65 \times 10^{-06} \times T^{-7.62} \exp(3509/T)$			
201	$\text{C}_2\text{H}_3 + \text{H}(+\text{M}) \leftrightarrow \text{C}_2\text{H}_4(+\text{M})$	$1.01 \times 10^{-11} \times T^{0.27} \exp(-141/T)$	[36]
Third-body efficiencies H_2O 5.0, H_2 2.0, CO_2 3.0, CO 2.0			
Troe parameters: $a = 0.782$, $T^{***} = 208.0$, $T^* = 2663.0$, $T^{**} = 6095.0$			
Rate coefficient for low pressure limit ($\text{cm}^3 \text{s}^{-1}$): $2.70 \times 10^{-18} \times T^{-3.86} \exp(1671/T)$			

Table 1. (Continued.)

N	Reaction	Rate coefficient (s^{-1} or $\text{cm}^3 \text{s}^{-1}$ or $\text{cm}^6 \text{s}^{-1}$)	Ref.
202	$\text{C}_2\text{H}_3 + \text{O} \leftrightarrow \text{CH}_2\text{CO} + \text{H}$	4.98×10^{-11}	[36]
203	$\text{C}_2\text{H}_3 + \text{O}_2 \leftrightarrow \text{CH}_2\text{O} + \text{HCO}$	$2.82 \times 10^{05} \times T^{-5.31} \exp(3272/T)$	[35]
204	$\text{C}_2\text{H}_3 + \text{O}_2 \leftrightarrow \text{CH}_2\text{HCO} + \text{O}$	$9.13 \times 10^{-10} \times T^{-0.61} \exp(2648/T)$	[35]
205	$\text{C}_2\text{H}_3 + \text{CH}_3 \leftrightarrow \text{C}_3\text{H}_5(\text{a}) + \text{H}$	4.00×10^{-12}	[35]
206	$\text{C}_2\text{H}_3 + \text{CH}_3 \leftrightarrow \text{C}_3\text{H}_6$	$7.41 \times 10^{32} \times T^{-13.00} \exp(6980/T)$	[39]
207	$\text{HCCOH} + \text{H} \leftrightarrow \text{CH}_2\text{CO} + \text{H}$	1.66×10^{-11}	[35]
208	$\text{CH}_2\text{HCO} + \text{H} \leftrightarrow \text{CH}_3 + \text{HCO}$	8.30×10^{-11}	[39]
209	$\text{CH}_2\text{HCO} + \text{H} \leftrightarrow \text{CH}_2\text{CO} + \text{H}_2$	3.32×10^{-11}	[39]
210	$\text{CH}_2\text{HCO} + \text{O} \leftrightarrow \text{CH}_2\text{O} + \text{HCO}$	1.66×10^{-10}	[39]
211	$\text{CH}_2\text{HCO} + \text{OH} \leftrightarrow \text{CH}_2\text{CO} + \text{H}_2\text{O}$	4.98×10^{-11}	[39]
212	$\text{CH}_2\text{HCO} + \text{O}_2 \rightarrow \text{CH}_2\text{O} + \text{CO} + \text{OH}$	4.98×10^{-14}	[35]
213	$\text{CH}_2\text{HCO} + \text{CH}_3 \rightarrow \text{C}_2\text{H}_5 + \text{CO} + \text{H}$	$8.14 \times 10^{-10} \times T^{-0.50}$	[39]
214	$\text{CH}_2\text{HCO} + \text{HO}_2 \rightarrow \text{CH}_2\text{O} + \text{HCO} + \text{OH}$	1.16×10^{-11}	[39]
215	$\text{CH}_2\text{HCO} + \text{HO}_2 \leftrightarrow \text{CH}_3\text{HCO} + \text{O}_2$	4.98×10^{-12}	[39]
216	$\text{CH}_2\text{HCO} \rightarrow \text{CH}_3 + \text{CO}$	$1.17 \times 10^{43} \times T^{-9.83} \exp(22028/T)$	[39]
217	$\text{CH}_2\text{HCO} \rightarrow \text{CH}_2\text{CO} + \text{H}$	$1.81 \times 10^{43} \times T^{-9.61} \exp(23092/T)$	[39]
218	$\text{CHOCHO}(\text{+M}) \leftrightarrow \text{CH}_2\text{O} + \text{CO}(\text{+M})$	$4.27 \times 10^{12} \times \exp(-25474/T)$	[38]
Rate coefficient for low pressure limit ($\text{cm}^3 \text{s}^{-1}$): $1.48 \times 10^{-07} \times \exp(-24769/T)$			
219	$\text{CHOCHO} \rightarrow \text{CO} + \text{CO} + \text{H}_2$	$4.07 \times 10^{42} \times T^{-8.50} \exp(34877/T)$	[38]
220	$\text{CHOCHO} + \text{OH} \rightarrow \text{HCO} + \text{CO} + \text{H}_2\text{O}$	1.66×10^{-11}	[38]
221	$\text{CHOCHO} + \text{O} \rightarrow \text{HCO} + \text{CO} + \text{OH}$	$1.20 \times 10^{-11} \times \exp(-992/T)$	[38]
222	$\text{CHOCHO} + \text{H} \leftrightarrow \text{CH}_2\text{O} + \text{HCO}$	1.66×10^{-12}	[38]
223	$\text{CHOCHO} + \text{HO}_2 \rightarrow \text{HCO} + \text{CO} + \text{H}_2\text{O}_2$	$2.82 \times 10^{-12} \times \exp(-5387/T)$	[38]
224	$\text{CHOCHO} + \text{CH}_3 \rightarrow \text{HCO} + \text{CO} + \text{CH}_4$	$2.89 \times 10^{-12} \times \exp(-4249/T)$	[38]
225	$\text{CHOCHO} + \text{O}_2 \rightarrow \text{HCO} + \text{CO} + \text{HO}_2$	$1.66 \times 10^{-10} \times \exp(-18627/T)$	[38]
226	$\text{CH}_3\text{CO}(\text{+M}) \leftrightarrow \text{CH}_3 + \text{CO}(\text{+M})$	$3.00 \times 10^{12} \times \exp(-8418/T)$	[35]
Rate coefficient for low pressure limit ($\text{cm}^3 \text{s}^{-1}$): $1.99 \times 10^{-09} \times \exp(-6302/T)$			
227	$\text{CH}_2\text{CO} + \text{O} \leftrightarrow \text{CO}_2 + \text{CH}_2$	$2.91 \times 10^{-12} \times \exp(-680/T)$	[35]
228	$\text{CH}_2\text{CO} + \text{H} \leftrightarrow \text{CH}_3 + \text{CO}$	$4.50 \times 10^{-20} \times T^{2.75} \exp(-359/T)$	[39]
229	$\text{CH}_2\text{CO} + \text{H} \leftrightarrow \text{HCCO} + \text{H}_2$	$3.32 \times 10^{-10} \times \exp(-4027/T)$	[39]
230	$\text{CH}_2\text{CO} + \text{O} \leftrightarrow \text{HCCO} + \text{OH}$	$1.66 \times 10^{-11} \times \exp(-4027/T)$	[35]
231	$\text{CH}_2\text{CO} + \text{OH} \leftrightarrow \text{HCCO} + \text{H}_2\text{O}$	$1.66 \times 10^{-11} \times \exp(-1007/T)$	[39]
232	$\text{CH}_2\text{CO} + \text{OH} \leftrightarrow \text{CH}_2\text{OH} + \text{CO}$	$6.19 \times 10^{-12} \times \exp(510/T)$	[35]
233	$\text{CH}_2\text{CO}(\text{+M}) \leftrightarrow \text{CH}_2 + \text{CO}(\text{+M})$	$3.00 \times 10^{14} \times \exp(-35734/T)$	[35]
Rate coefficient for low pressure limit ($\text{cm}^3 \text{s}^{-1}$): $5.98 \times 10^{-09} \times \exp(-29839/T)$			
234	$\text{C}_2\text{H} + \text{O} \leftrightarrow \text{CH} + \text{CO}$	8.30×10^{-11}	[35]
235	$\text{C}_2\text{H} + \text{OH} \leftrightarrow \text{HCCO} + \text{H}$	3.32×10^{-11}	[35]
236	$\text{C}_2\text{H} + \text{O}_2 \rightarrow \text{CO} + \text{CO} + \text{H}$	$1.50 \times 10^{-11} \times \exp(230/T)$	[35]
237	$\text{HCCO} + \text{H} \leftrightarrow \text{CH}_2(\text{s}) + \text{CO}$	1.66×10^{-10}	[35]
238	$\text{HCCO} + \text{O} \rightarrow \text{H} + \text{CO} + \text{CO}$	1.33×10^{-10}	[35]
239	$\text{HCCO} + \text{O} \leftrightarrow \text{CH} + \text{CO}_2$	$4.90 \times 10^{-11} \times \exp(-560/T)$	[35]
240	$\text{HCCO} + \text{O}_2 \rightarrow \text{HCO} + \text{CO} + \text{O}$	$4.15 \times 10^{-16} \times T$	[35]
241	$\text{HCCO} + \text{O}_2 \leftrightarrow \text{CO}_2 + \text{HCO}$	$3.99 \times 10^{-13} \times \exp(430/T)$	[35]
242	$\text{HCCO} + \text{OH} \leftrightarrow \text{C}_2\text{O} + \text{H}_2\text{O}$	4.98×10^{-11}	[35]
243	$\text{C}_2\text{O} + \text{H} \leftrightarrow \text{CH} + \text{CO}$	1.66×10^{-11}	[35]
244	$\text{C}_2\text{O} + \text{O} \leftrightarrow \text{CO} + \text{CO}$	8.30×10^{-11}	[35]
245	$\text{C}_2\text{O} + \text{OH} \rightarrow \text{CO} + \text{CO} + \text{H}$	3.32×10^{-11}	[35]
246	$\text{C}_2\text{O} + \text{O}_2 \rightarrow \text{CO} + \text{CO} + \text{O}$	3.32×10^{-11}	[35]
C ₃ hydrocarbon submechanism			
247	$\text{C}_3\text{H}_8(\text{+M}) \leftrightarrow \text{C}_2\text{H}_5 + \text{CH}_3(\text{+M})$	$7.90 \times 10^{22} \times T^{-1.80} \times \exp(44619/T)$	[35]
Third-body efficiencies H ₂ O 5.0, H ₂ 2.0, CO ₂ 3.0, CO 2.0			
Troé parameters: $a = 1.0$, $T^{***} = 10^{-15}$, $T^* = 1500.0$, $T^{**} = 10^{15}$			
Rate coefficient for low pressure limit ($\text{cm}^3 \text{s}^{-1}$): $1.20 \times 10^{04} \times T^{-2.88} \exp(33956/T)$			

(Continued)

Table 1. (Continued.)

N	Reaction	Rate coefficient (s^{-1} or $\text{cm}^3 \text{s}^{-1}$ or $\text{cm}^6 \text{s}^{-1}$)	Ref.
248	$\text{C}_3\text{H}_7(\text{i}) + \text{HO}_2 \leftrightarrow \text{C}_3\text{H}_8 + \text{O}_2$	4.98×10^{-12}	[40]
249	$\text{C}_3\text{H}_7(\text{n}) + \text{HO}_2 \leftrightarrow \text{C}_3\text{H}_8 + \text{O}_2$	4.98×10^{-12}	[39]
250	$\text{C}_3\text{H}_8 + \text{HO}_2 \leftrightarrow \text{C}_3\text{H}_7(\text{n}) + \text{H}_2\text{O}_2$	$7.90 \times 10^{-20} \times T^{2.55} \exp(-8303/T)$	[40]
251	$\text{C}_3\text{H}_8 + \text{HO}_2 \leftrightarrow \text{C}_3\text{H}_7(\text{i}) + \text{H}_2\text{O}_2$	$1.60 \times 10^{-20} \times T^{2.60} \exp(-7002/T)$	[40]
252	$\text{C}_3\text{H}_8 + \text{OH} \leftrightarrow \text{C}_3\text{H}_7(\text{n}) + \text{H}_2\text{O}$	$5.25 \times 10^{-17} \times T^{1.80} \exp(-470/T)$	[35]
253	$\text{C}_3\text{H}_8 + \text{OH} \leftrightarrow \text{C}_3\text{H}_7(\text{i}) + \text{H}_2\text{O}$	$1.18 \times 10^{-17} \times T^{1.90} \exp(80/T)$	[35]
254	$\text{C}_3\text{H}_8 + \text{O} \leftrightarrow \text{C}_3\text{H}_7(\text{n}) + \text{OH}$	$\min(6.19 \times 10^{-18} \times T^{2.40} \exp(-2771/T), 10^{-9})$	[35]
255	$\text{C}_3\text{H}_8 + \text{O} \leftrightarrow \text{C}_3\text{H}_7(\text{i}) + \text{OH}$	$9.10 \times 10^{-19} \times T^{2.50} \exp(-1580/T)$	[35]
257	$\text{C}_3\text{H}_8 + \text{H} \leftrightarrow \text{C}_3\text{H}_7(\text{i}) + \text{H}_2$	$2.16 \times 10^{-18} \times T^{2.40} \exp(-2251/T)$	[40]
258	$\text{C}_3\text{H}_8 + \text{H} \leftrightarrow \text{C}_3\text{H}_7(\text{n}) + \text{H}_2$	$\min(2.21 \times 10^{-18} \times T^{2.54} \exp(-3401/T), 10^{-9})$	[40]
259	$\text{C}_3\text{H}_8 + \text{CH}_3 \leftrightarrow \text{C}_3\text{H}_7(\text{n}) + \text{CH}_4$	$1.50 \times 10^{-24} \times T^{3.65} \exp(-3601/T)$	[40]
260	$\text{C}_3\text{H}_8 + \text{CH}_3 \leftrightarrow \text{C}_3\text{H}_7(\text{i}) + \text{CH}_4$	$2.51 \times 10^{-24} \times T^{3.46} \exp(-2759/T)$	[40]
261	$\text{C}_3\text{H}_8 + \text{C}_2\text{H}_3 \leftrightarrow \text{C}_3\text{H}_7(\text{i}) + \text{C}_2\text{H}_4$	$1.66 \times 10^{-21} \times T^{3.10} \exp(-4445/T)$	[40]
262	$\text{C}_3\text{H}_8 + \text{C}_2\text{H}_3 \leftrightarrow \text{C}_3\text{H}_7(\text{n}) + \text{C}_2\text{H}_4$	$9.96 \times 10^{-22} \times T^{3.30} \exp(-5286/T)$	[40]
263	$\text{C}_3\text{H}_8 + \text{C}_2\text{H}_5 \leftrightarrow \text{C}_3\text{H}_7(\text{i}) + \text{C}_2\text{H}_6$	$2.51 \times 10^{-24} \times T^{3.46} \exp(-3761/T)$	[40]
264	$\text{C}_3\text{H}_8 + \text{C}_2\text{H}_5 \leftrightarrow \text{C}_3\text{H}_7(\text{n}) + \text{C}_2\text{H}_6$	$1.50 \times 10^{-24} \times T^{3.65} \exp(-4601/T)$	[40]
265	$\text{C}_3\text{H}_8 + \text{C}_3\text{H}_5(\text{a}) \leftrightarrow \text{C}_3\text{H}_6 + \text{C}_3\text{H}_7(\text{n})$	$3.90 \times 10^{-22} \times T^{3.30} \exp(-9989/T)$	[40]
266	$\text{C}_3\text{H}_8 + \text{C}_3\text{H}_5(\text{a}) \leftrightarrow \text{C}_3\text{H}_6 + \text{C}_3\text{H}_7(\text{i})$	$1.30 \times 10^{-22} \times T^{3.30} \exp(-9147/T)$	[40]
267	$\text{C}_3\text{H}_7(\text{n})(+\text{M}) \leftrightarrow \text{C}_2\text{H}_4 + \text{CH}_3(+\text{M})$	$1.23 \times 10^{13} \times T^{-0.10} \exp(15205/T)$	[35]
Third-body efficiencies H_2O 5.0, H_2 2.0, CO_2 3.0, CO 2.0			
Troé parameters: $a = 2.17$, $T^{***} = 10^{-15}$, $T^* = 251.0$, $T^{**} = 1185.0$			
Rate coefficient for low pressure limit ($\text{cm}^3 \text{s}^{-1}$): $9.11 \times 10^{25} \times T^{-10.0} \times \exp(18006/T)$			
268	$\text{C}_3\text{H}_6 + \text{H}(+\text{M}) \leftrightarrow \text{C}_3\text{H}_7(\text{i})(+\text{M})$	$9.47 \times 10^{-15} \times T^{1.16} \exp(-440/T)$	[35]
Third-body efficiencies H_2O 5.0, H_2 2.0, CO_2 3.0, CO 2.0			
Troé parameters: $a = 1.0$, $T^{***} = 10^{-15}$, $T^* = 260.0$, $T^{**} = 3000.0$			
Rate coefficient for low pressure limit ($\text{cm}^3 \text{s}^{-1}$): $4.52 \times 10^{06} \times T^{-11.10} \exp(4714/T)$			
269	$\text{C}_3\text{H}_7(\text{i}) + \text{O}_2 \leftrightarrow \text{C}_3\text{H}_6 + \text{HO}_2$	$3.12 \times 10^{-04} \times T^{-2.69} \exp(3579/T)$	[35]
270	$\text{C}_3\text{H}_7(\text{n}) + \text{O}_2 \leftrightarrow \text{C}_3\text{H}_6 + \text{HO}_2$	$6.36 \times 10^{02} \times T^{-4.44} \exp(3889/T)$	[39]
271	$\text{C}_3\text{H}_7(\text{i}) + \text{H} \leftrightarrow \text{C}_2\text{H}_5 + \text{CH}_3$	8.30×10^{-11}	[40]
272	$\text{C}_3\text{H}_7(\text{n}) + \text{H} \leftrightarrow \text{C}_2\text{H}_5 + \text{CH}_3$	1.66×10^{-10}	[40]
273	$\text{C}_3\text{H}_6 \rightarrow \text{C}_2\text{H}_2 + \text{CH}_4$	$2.50 \times 10^{12} \times \exp(-35240/T)$	[35]
274	$\text{C}_3\text{H}_6 \rightarrow \text{C}_3\text{H}_4(\text{a}) + \text{H}_2$	$3.00 \times 10^{13} \times \exp(-40275/T)$	[35]
275	$\text{C}_3\text{H}_5(\text{p}) + \text{H} \rightarrow \text{C}_3\text{H}_6$	1.66×10^{-10}	[39]
276	$\text{C}_3\text{H}_5(\text{s}) + \text{H} \rightarrow \text{C}_3\text{H}_6$	1.66×10^{-10}	[39]
277	$\text{C}_3\text{H}_6 + \text{HO}_2 \leftrightarrow \text{C}_3\text{H}_5(\text{a}) + \text{H}_2\text{O}_2$	$1.60 \times 10^{-20} \times T^{2.60} \exp(-7003/T)$	[40]
278	$\text{C}_3\text{H}_6 + \text{OH} \leftrightarrow \text{C}_3\text{H}_5(\text{a}) + \text{H}_2\text{O}$	$5.18 \times 10^{-18} \times T^{2.00} \exp(150/T)$	[40]
279	$\text{C}_3\text{H}_6 + \text{OH} \leftrightarrow \text{C}_3\text{H}_5(\text{s}) + \text{H}_2\text{O}$	$1.84 \times 10^{-18} \times T^{2.00} \exp(-730/T)$	[40]
280	$\text{C}_3\text{H}_6 + \text{OH} \leftrightarrow \text{C}_3\text{H}_5(\text{p}) + \text{H}_2\text{O}$	$3.50 \times 10^{-18} \times T^{2.00} \exp(-1399/T)$	[40]
281	$\text{C}_3\text{H}_6 + \text{O} \rightarrow \text{CH}_3\text{CHCO} + \text{H} + \text{H}$	$8.32 \times 10^{-17} \times T^{1.76} \exp(-38/T)$	[40]
282	$\text{C}_3\text{H}_6 + \text{O} \leftrightarrow \text{C}_2\text{H}_5 + \text{HCO}$	$2.62 \times 10^{-17} \times T^{1.76} \exp(612/T)$	[40]
283	$\text{C}_3\text{H}_6 + \text{O} \leftrightarrow \text{C}_3\text{H}_5(\text{a}) + \text{OH}$	$8.70 \times 10^{-13} \times T^{0.70} \exp(-2962/T)$	[40]
284	$\text{C}_3\text{H}_6 + \text{O} \leftrightarrow \text{C}_3\text{H}_5(\text{p}) + \text{OH}$	$1.99 \times 10^{-13} \times T^{0.70} \exp(-4510/T)$	[40]
285	$\text{C}_3\text{H}_6 + \text{O} \leftrightarrow \text{C}_3\text{H}_5(\text{s}) + \text{OH}$	$1.00 \times 10^{-13} \times T^{0.70} \exp(-3842/T)$	[40]
286	$\text{C}_3\text{H}_6 + \text{H} \leftrightarrow \text{C}_2\text{H}_4 + \text{CH}_3$	$1.20 \times 10^{-11} \times \exp(-655/T)$	[40]
287	$\text{C}_3\text{H}_6 + \text{H} \leftrightarrow \text{C}_3\text{H}_5(\text{a}) + \text{H}_2$	$2.87 \times 10^{-19} \times T^{2.50} \exp(-1255/T)$	[40]
288	$\text{C}_3\text{H}_6 + \text{H} \leftrightarrow \text{C}_3\text{H}_5(\text{s}) + \text{H}_2$	$6.79 \times 10^{-19} \times T^{2.50} \exp(-4931/T)$	[40]
289	$\text{C}_3\text{H}_6 + \text{H} \leftrightarrow \text{C}_3\text{H}_5(\text{p}) + \text{H}_2$	$1.34 \times 10^{-18} \times T^{2.50} \exp(-6184/T)$	[40]
290	$\text{C}_3\text{H}_5(\text{a}) + \text{HO}_2 \leftrightarrow \text{C}_3\text{H}_6 + \text{O}_2$	4.98×10^{-12}	[40]
291	$\text{C}_3\text{H}_6 + \text{CH}_3 \leftrightarrow \text{C}_3\text{H}_5(\text{a}) + \text{CH}_4$	$3.69 \times 10^{-24} \times T^{3.50} \exp(-2857/T)$	[40]
292	$\text{C}_3\text{H}_6 + \text{CH}_3 \leftrightarrow \text{C}_3\text{H}_5(\text{s}) + \text{CH}_4$	$1.40 \times 10^{-24} \times T^{3.50} \exp(-5868/T)$	[40]
293	$\text{C}_3\text{H}_6 + \text{CH}_3 \leftrightarrow \text{C}_3\text{H}_5(\text{p}) + \text{CH}_4$	$2.24 \times 10^{-24} \times T^{3.50} \exp(-6468/T)$	[40]
294	$\text{C}_3\text{H}_6 + \text{HCO} \leftrightarrow \text{C}_3\text{H}_5(\text{a}) + \text{CH}_2\text{O}$	$1.79 \times 10^{-17} \times T^{1.90} \exp(-8563/T)$	[40]
295	$\text{CH}_3\text{CHCO} + \text{OH} \leftrightarrow \text{CH}_2\text{CHCO} + \text{H}_2\text{O}$	$6.64 \times 10^{-18} \times T^{2.00}$	[39]

Table 1. (Continued.)

N	Reaction	Rate coefficient (s^{-1} or $cm^3 s^{-1}$ or $cm^6 s^{-1}$)	Ref.
296	$CH_3CHCO + O \leftrightarrow CH_2CHCO + OH$	$1.26 \times 10^{-15} \times T^{1.50} \exp(-4279/T)$	[39]
297	$CH_3CHCO + H \leftrightarrow CH_2CHCO + H_2$	$3.32 \times 10^{-19} \times T^{2.50} \exp(-1259/T)$	[39]
298	$CH_3CHCO + H \leftrightarrow C_2H_5 + CO$	$3.32 \times 10^{-11} \times \exp(-1007/T)$	[39]
299	$CH_3CHCO + O \rightarrow CH_3 + HCO + CO$	$4.98 \times 10^{-17} \times T^{2.00}$	[39]
300	$CH_2CHCHO + OH \leftrightarrow CH_2CHCO + H_2O$	1.66×10^{-11}	[39]
301	$CH_2CHCHO + O \leftrightarrow CH_2CHCO + OH$	$1.20 \times 10^{-11} \times \exp(-992/T)$	[39]
302	$CH_2CHCHO + O \rightarrow CH_2CO + HCO + H$	$8.32 \times 10^{-17} \times T^{1.76} \times \exp(-38/T)$	[39]
303	$CH_2CHCHO + H \leftrightarrow CH_2CHCO + H_2$	$6.61 \times 10^{-11} \times \exp(-2114/T)$	[39]
304	$CH_2CHCHO + H \leftrightarrow C_2H_4 + HCO$	$3.32 \times 10^{-11} \times \exp(-1762/T)$	[39]
305	$CH_2CHCHO + O_2 \leftrightarrow CH_2CHCO + HO_2$	$4.98 \times 10^{-11} \times \exp(-18124/T)$	[39]
306	$C_2H_3 + CO \leftrightarrow CH_2CHCO$	$2.51 \times 10^{-13} \times \exp(-2422/T)$	[40]
307	$CH_2CHCO + O \leftrightarrow C_2H_3 + CO_2$	1.66×10^{-10}	[39]
308	$C_3H_5(a) + O_2 \leftrightarrow CH_2CHCHO + OH$	$3.02 \times 10^{-11} \times T^{-0.41} \exp(11508/T)$	[35]
309	$C_3H_5(a) + O_2 \leftrightarrow C_3H_4(a) + HO_2$	$8.29 \times 10^{-09} \times T^{-1.40} \exp(11291/T)$	[35]
310	$C_3H_5(a) + O_2 \leftrightarrow CH_2HCO + CH_2O$	$1.76 \times 10^{-14} \times T^{0.34} \exp(-6463/T)$	[35]
311	$C_3H_5(a) + O_2 \rightarrow C_2H_2 + CH_2O + OH$	$4.62 \times 10^{01} \times T^{-4.80} \exp(7787/T)$	[35]
312	$C_3H_5(a) + OH \leftrightarrow C_3H_4(a) + H_2O$	1.66×10^{-11}	[40]
313	$C_3H_5(a) + H \leftrightarrow C_3H_4(a) + H_2$	8.30×10^{-11}	[40]
314	$C_3H_5(a) + H \leftrightarrow C_3H_6$	$3.12 \times 10^{02} \times T^{-3.60} \exp(2753/T)$	[39]
315	$C_3H_5(a) + O \leftrightarrow CH_2CHCHO + H$	3.01×10^{-10}	[35]
316	$C_3H_5(a) + CH_3 \leftrightarrow C_3H_4(a) + CH_4$	$5.01 \times 10^{-12} \times \exp(66/T)$	[40]
317	$C_3H_5(p) + O_2 \leftrightarrow CH_3HCO + HCO$	$1.81 \times 10^{-01} \times T^{-3.29} \exp(1959/T)$	[39]
318	$C_3H_5(p) + O_2 \rightarrow CH_3CHCO + H + O$	$2.66 \times 10^{-09} \times T^{-0.78} \exp(1578/T)$	[39]
319	$C_3H_5(p) + O \leftrightarrow CH_3CHCO + H$	1.66×10^{-10}	[39]
320	$C_3H_5(p) + H \leftrightarrow C_3H_4(p) + H_2$	3.32×10^{-11}	[39]
321	$C_3H_5(p) + OH \leftrightarrow C_3H_4(p) + H_2O$	1.66×10^{-11}	[39]
322	$C_3H_5(p) + H \leftrightarrow C_3H_5(a) + H$	1.66×10^{-10}	[39]
323	$C_3H_5(s) + H \leftrightarrow C_3H_5(a) + H$	1.66×10^{-10}	[39]
324	$C_3H_5(s) + O_2 \leftrightarrow CH_3CO + CH_2O$	$1.81 \times 10^{-02} \times T^{-3.29} \exp(1959/T)$	[39]
325	$C_3H_5(s) + O \leftrightarrow CH_2CO + CH_3$	1.66×10^{-10}	[39]
326	$C_3H_5(s) + H \leftrightarrow C_3H_4(p) + H_2$	6.64×10^{-11}	[39]
327	$C_3H_5(s) + OH \leftrightarrow C_3H_4(p) + H_2O$	3.32×10^{-11}	[39]
328	$C_3H_4(a) + H \leftrightarrow H_2CCCH + H_2$	$3.32 \times 10^{-17} \times T^{2.00} \exp(-2517/T)$	[35]
329	$C_3H_4(a) + O \leftrightarrow C_2H_4 + CO$	$2.23 \times 10^{-17} \times T^{1.88} \exp(-90/T)$	[39]
330	$C_3H_4(a) + OH \leftrightarrow H_2CCCH + H_2O$	$1.66 \times 10^{-17} \times T^{2.00} \exp(-503/T)$	[35]
331	$C_3H_4(a) + CH_3 \leftrightarrow H_2CCCH + CH_4$	$2.49 \times 10^{-24} \times T^{3.50} \exp(-2819/T)$	[35]
332	$C_3H_4(a) \leftrightarrow C_3H_4(p)$	$1.48 \times 10^{13} \times \exp(-30408/T)$	[35]
333	$C_3H_4(p) + H \leftrightarrow H_2CCCH + H_2$	$3.32 \times 10^{-17} \times T^{2.00} \exp(-2517/T)$	[35]
334	$C_3H_4(p) + O \leftrightarrow C_2H_4 + CO$	$2.49 \times 10^{-11} \times \exp(-1058/T)$	[39]
335	$C_3H_4(p) + OH \leftrightarrow H_2CCCH + H_2O$	$1.66 \times 10^{-17} \times T^{2.00} \exp(-503/T)$	[35]
336	$C_3H_4(p) + CH_3 \leftrightarrow H_2CCCH + CH_4$	$2.49 \times 10^{-24} \times T^{3.50} \exp(-2819/T)$	[35]
337	$C_3H_4(p) + H(+M) \leftrightarrow C_3H_5(s)(+M)$	$1.08 \times 10^{-11} \times \exp(-1007/T)$	[35]
	Rate coefficient for low pressure limit ($cm^3 s^{-1}$): $2.33 \times 10^{-08} \times T^{-7.27} \exp(3311/T)$		
338	$C_3H_4(a) + H(+M) \leftrightarrow C_3H_5(a)(+M)$	$1.99 \times 10^{-13} \times T^{0.69} \exp(-1514/T)$	[35]
	Rate coefficient for low pressure limit ($cm^3 s^{-1}$): $1.53 \times 10^{-14} \times T^{-5.00} \exp(2239/T)$		
339	$C_3H_4(a) + H(+M) \leftrightarrow C_3H_5(s)(+M)$	$1.41 \times 10^{-11} \times \exp(-1007/T)$	[35]
	Rate coefficient for low pressure limit ($cm^3 s^{-1}$): $3.06 \times 10^{-14} \times T^{-5.00} \exp(2239/T)$		
340	$H_2CCCH + O_2 \leftrightarrow CH_2CO + HCO$	$4.98 \times 10^{-14} \times \exp(-1444/T)$	[35]
341	$H_2CCCH + O \leftrightarrow CH_2O + C_2H$	2.32×10^{-10}	[24]
342	$H_2CCCH + H \leftrightarrow C_3H_2 + H_2$	$8.30 \times 10^{-11} \times \exp(-503/T)$	[35]
343	$H_2CCCH + OH \leftrightarrow C_3H_2 + H_2O$	3.32×10^{-11}	[35]
344	$H_2CCCH + CH_3 \leftrightarrow C_3H_2 + CH_4$	3.32×10^{-11}	[35]
345	$H_2CCCH + H(+M) \leftrightarrow C_3H_4(a)(+M)$	$2.76 \times 10^{-09} \times T^{-0.37}$	[39]

(Continued)

Table 1. (Continued.)

N	Reaction	Rate coefficient (s^{-1} or $cm^3 s^{-1}$ or $cm^6 s^{-1}$)	Ref.
Third-body efficiencies: H ₂ O 5.0, H ₂ 2.0, CO ₂ 3.0, CO 2.0, O ₂ 2.0, C ₂ H ₂ 2.0			
Rate coefficient for low pressure limit ($cm^3 s^{-1}$): $9.27 \times 10^{-03} \times T^{-8.52} \exp(3168/T)$			
346	H ₂ CCCH + H(+M) ↔ C ₃ H ₄ (p)(+M)	$2.76 \times 10^{-09} \times T^{-0.37}$	[39]
Third-body efficiencies: H ₂ O 5.0, H ₂ 2.0, CO ₂ 3.0, CO 2.0, O ₂ 2.0, C ₂ H ₂ 2.0			
Rate coefficient for low pressure limit ($cm^3 s^{-1}$): $2.42 \times 10^{-02} \times T^{-8.90} \exp(4014/T)$			
347	C ₃ H ₂ + O ₂ → HCCO + CO + H	$3.32 \times 10^{-12} \times \exp(-503/T)$	[39]
348	CH ₂ + CH ₂ → C ₂ H ₂ + H + H	$3.32 \times 10^{-10} \times \exp(-5532/T)$	[36]
349	CH ₂ + C ₂ H ₂ ↔ H ₂ CCCH + H	$1.99 \times 10^{-11} \times \exp(-3323/T)$	[35]
350	CH ₂ (s) + C ₂ H ₂ ↔ H ₂ CCCH + H	2.49×10^{-10}	[35]
351	CH + C ₂ H ₂ ↔ C ₃ H ₂ + H	1.66×10^{-10}	[35]
352	CH + CH ₂ ↔ C ₂ H ₂ + H	6.64×10^{-11}	[35]
353	C ₂ H ₄ (+M) ↔ C ₂ H ₂ + H ₂ (+M)	$1.80 \times 10^{14} \times \exp(-43799/T)$	[35]
Rate coefficient for low pressure limit ($cm^3 s^{-1}$): $2.49 \times 10^{-09} \times \exp(-27912/T)$			
354	C ₂ H ₃ + H ↔ C ₂ H ₂ + H ₂	1.49×10^{-10}	[35]
355	C ₂ H ₃ + O ₂ ↔ C ₂ H ₂ + HO ₂	$2.22 \times 10^{-18} \times T^{1.61} \exp(193/T)$	[36]
356	C ₂ H ₃ + OH ↔ C ₂ H ₂ + H ₂ O	3.32×10^{-11}	[35]
357	C ₂ H ₃ + C ₂ H ↔ C ₂ H ₂ + C ₂ H ₂	4.98×10^{-11}	[35]
358	C ₂ H ₃ + CH ↔ CH ₂ + C ₂ H ₂	8.30×10^{-11}	[35]
359	C ₂ H ₃ + CH ₃ ↔ C ₂ H ₂ + CH ₄	3.32×10^{-11}	[35]
360	C ₂ H ₂ + OH ↔ C ₂ H + H ₂ O	$5.60 \times 10^{-17} \times T^{2.00} \exp(-7048/T)$	[35]
361	C ₂ H ₂ + OH ↔ HCCOH + H	$8.37 \times 10^{-19} \times T^{2.30} \exp(-6796/T)$	[35]
362	C ₂ H ₂ + OH ↔ CH ₂ CO + H	$3.62 \times 10^{-28} \times T^{4.50} \exp(503/T)$	[35]
363	C ₂ H ₂ + OH ↔ CH ₂ CO + H	3.32×10^{-13}	[35]
364	C ₂ H ₂ + OH ↔ CH ₃ + CO	$8.02 \times 10^{-28} \times T^{4.00} \exp(1007/T)$	[35]
365	C ₂ H ₂ + O ↔ CH ₂ + CO	$1.02 \times 10^{-17} \times T^{2.00} \exp(-957/T)$	[39]
366	C ₂ H ₂ + O ↔ HCCO + H	$2.38 \times 10^{-17} \times T^{2.00} \exp(-957/T)$	[39]
367	O + C ₂ H ₂ ↔ OH + C ₂ H	$7.64 \times 10^{-05} \times T^{-1.41} \exp(14574/T)$	[36]
368	C ₂ H ₂ + CH ₃ ↔ C ₂ H + CH ₄	$3.01 \times 10^{-13} \times \exp(-8704/T)$	[35]
369	C ₂ H ₂ + O ₂ ↔ HCCO + OH	$6.64 \times 10^{-17} \times T^{1.50} \exp(-15153/T)$	[35]
370	H + C ₂ H(+M) ↔ C ₂ H ₂ (+M)	$1.66 \times 10^{-07} \times T^{-1.00}$	[36]
Third-body efficiencies: H ₂ 2.0, H ₂ O 6.0, CH ₄ 2.0, CO 1.5, CO ₂ 2.0, C ₂ H ₆ 3.0, Ar 0.7			
Troe parameters: $a = 6464$ $T^{***} = 132.00$ $T^* = 1315.00$ $T^{**} = 5566.00$			
Rate coefficient for low pressure limit ($cm^3 s^{-1}$): $1.03 \times 10^{-14} \times T^{-4.80} \times \exp(957/T)$			
371	H + C ₂ H ₂ (+M) ↔ C ₂ H ₃ (+M)	$9.30 \times 10^{-12} \times \exp(-1208/T)$	[36]
Third-body efficiencies: H ₂ 2.0, H ₂ O 6.0, CH ₄ 2.0, CO 1.5, CO ₂ 2.0, C ₂ H ₆ 3.0, Ar 0.7			
Troe parameters: $a = 0.7507$, $T^{***} = 98.50$, $T^* = 1302.00$, $T^{**} = 4167.00$			
Rate coefficient for low pressure limit ($cm^3 s^{-1}$): $1.05 \times 10^{-07} \times T^{-7.27} \exp(3635/T)$			
372	C ₂ H + H ₂ ↔ C ₂ H ₂ + H	$6.79 \times 10^{-19} \times T^{2.39} \exp(-435/T)$	[36]
373	HCCO + C ₂ H ₂ ↔ H ₂ CCCH + CO	$1.66 \times 10^{-13} \times \exp(-1510/T)$	[35]
374	HCCO + CH ↔ C ₂ H ₂ + CO	8.30×10^{-11}	[35]
375	HCCO + HCCO → C ₂ H ₂ + CO + CO	1.66×10^{-11}	[35]
376	C ₃ H ₄ (p) + H ↔ CH ₃ + C ₂ H ₂	$8.50 \times 10^{-14} \times T \times \exp(-1037/T)$	[35]
377	C ₃ H ₂ + O ↔ C ₂ H ₂ + CO	1.66×10^{-10}	[35]
378	C ₃ H ₂ + OH ↔ C ₂ H ₂ + HCO	8.30×10^{-11}	[35]
Carbonic – dicarbon submechanism			
379	C ₂ H + OH ↔ C ₂ + H ₂ O	$\min(6.64 \times 10^{-17} \times T^2 \exp(-4027/T), 5 \times 10^{-11})$	[37]
380	C + OH ↔ CO + H	8.30×10^{-11}	[37]
381	C + O ₂ ↔ CO + O	$1.99 \times 10^{-10} \times \exp(-2014/T)$	[37]
382	C + CH ₂ ↔ C ₂ H + H	8.30×10^{-11}	[37]
383	C ₂ + H ₂ ↔ C ₂ H + H	$1.10 \times 10^{-10} \times \exp(-4002/T)$	[37]
384	C ₂ + O ↔ C + CO	5.98×10^{-10}	[37]
385	C ₂ + O ₂ ↔ CO + CO	$1.49 \times 10^{-11} \times \exp(-493/T)$	[37]

Table 1. (Continued.)

N	Reaction	Rate coefficient (s^{-1} or $\text{cm}^3 \text{s}^{-1}$ or $\text{cm}^6 \text{s}^{-1}$)	Ref.
386	$\text{C}_2 + \text{OH} \leftrightarrow \text{C}_2\text{O} + \text{H}$	8.30×10^{-11}	[37]
387	$\text{H}_2\text{O} + \text{C} \leftrightarrow \text{CH} + \text{OH}$	$1.30 \times 10^{-12} \times T^{0.67} \exp(-19785/T)$	[37]
388	$\text{CH} + \text{CH} \leftrightarrow \text{C}_2 + \text{H}_2$	8.30×10^{-12}	[35]
389	$\text{CH}_2 + \text{M} \leftrightarrow \text{C} + \text{H}_2 + \text{M}$	$2.66 \times 10^{-10} \times \exp(-32220/T)$	[37]
390	$\text{CH} + \text{O} \leftrightarrow \text{C} + \text{OH}$	$2.52 \times 10^{-11} \times \exp(-2381/T)$	[37]
391	$\text{CH} + \text{H} \leftrightarrow \text{C} + \text{H}_2$	$1.31 \times 10^{-10} \times \exp(-81/T)$	[37]
392	$\text{C} + \text{CH}_3 \leftrightarrow \text{C}_2\text{H}_2 + \text{H}$	8.30×10^{-11}	[37]
393	$\text{C} + \text{C} + \text{M} \leftrightarrow \text{C}_2 + \text{M}$	$8.27 \times 10^{-34} \times \exp(503/T)$	[41]
394	$\text{C} + \text{CH} \leftrightarrow \text{C}_2 + \text{H}$	8.30×10^{-11}	[41]

Note:

1. Fall-off reaction in the Lindemann–Hinshelwood form: $k = k_0[M]/(1 + k_0[M]/k_\infty)$

2. Fall-off reaction in the Troe parameters form: $k = k_0[M]/(1 + k_0[M]/k_\infty)F$

$\ln F = (1 + (k/(N - d \times k))^2)^{-1} \ln F_{\text{cent}}; k = \ln(k_0[M]/k_\infty) + C$

$C = -0.4 - 0.67 \ln F_{\text{cent}}; N = 0.75 - 1.27 \ln F_{\text{cent}}; d = 0.14$

$F_{\text{cent}} = (1 - a) \exp(-T/T^{***}) + a \exp(-T/T^*) + \exp(-T^{**}/T)$

3. $\min(A, B)$ —minimum value between A and B .

where V_0 is the initial gas velocity [m s^{-1}], T_0 is the initial gas temperature, p_0 is the gas pressure, k_B is the Boltzmann's constant, $C_p = \frac{5}{2}k_B$ is the heat capacity at constant pressure, S is the plasma cross-section and P is the absorbed microwave power; δ is a coefficient expressing the fraction of absorbed power from the wave that is transferred to thermal energy of the gas. Here the electron energy balance equation is implicitly included via the coefficient δ . Given the fact that, under the conditions of interest, the main role of the electrons is to absorb microwave power and to transfer it to the heavy particles, we further assume $\delta = 0.9$, which is a typical value for atmospheric pressure conditions, and $\sim 10\%$ energy in radiation and dielectric losses. The approach used has been validated in a series of extensive experimental and theoretical studies [34, 49–54].

Under the present conditions, the contribution of the electrons to the ethanol dissociation kinetics is negligible, as the electron average energies are less than 1 eV and the degree of ionization is $\sim 10^{-4}$. The estimation based on the analyses of H-beta line demonstrates that the electron density in the middle of the plasma column is $\sim 10^{13} \text{ cm}^{-3}$, i.e. about five orders of magnitude less than the heavy particle density. Under conditions considered the local thermal equilibrium assumption can be justified [55]. Ar ions are the main positive ions in the plasma.

Considering the upper levels of the measured gas temperature, i.e. 2000 and 2200 K, the temperature profiles along the axis are shown in figure 4. The reference point $z = 0$ corresponds to the launcher position. The measured wall temperature axial profile (see figure 4(b)) as a boundary value of the gas temperature was fitted by an analytical expression and used as an external parameter in the numerical calculations [49]. The changes of wall temperature due to the external heating are shown by the broken line in the figure.

The fact that the gas temperature was considered to be radially inhomogeneous had a strong influence on the spatial dependence of the rate coefficients for reactions with high activation energy, E_a . In order to account for this effect in the

framework of a 1D model, the rate coefficients were radially averaged for every axial position z along the discharge length. Thus, effective rate coefficients k_{eff} were calculated as

$$k_{\text{eff}} = \frac{2}{R^2} \int_0^R k(T) r dr = \frac{2A}{R^2} \int_0^R T(r)^n \exp\left(-\frac{E_a}{T(r)}\right) r dr. \quad (4)$$

The rate of gas-phase carbon transformation into solid carbon corresponds to the diffusion transport rate of carbon atoms/molecules into a colder nucleation zone through the boundary of vaporization ($T \sim 1800 \text{ K}$) (figure 3). Since data for the diffusion coefficient of carbon species in argon plasma are not available in the literature, an estimation based on molecular kinetic theory was made [56]. According to the theory, the diffusion coefficient dependence on the temperature is $D = D_0 (T/T_0)^{3/2}$, where D_0 is the diffusion coefficient at temperature T_0 . Assuming that diffusion is the transport mechanism of gas-phase carbon species from the hot to the colder nucleation zone, and keeping in mind that the average distance $\sqrt{r^2}$ traveled by a particle within the time interval t is proportional to the square root of this time interval [56], it is readily found that the transformation rate is $k = \frac{1}{t} = \frac{6D_0}{r^2} (T/T_0)^{3/2}$ (s^{-1}). The schematic presentation of the isothermal plasma surface with constant temperature equal to 1800 K is shown in figure 3, and it is marked as ‘vaporization boundary.’ According to the equilibrium thermodynamic modeling (figure 5) the sublimation of solid carbon is observed in the temperature range 1700–2000 K. Hence we estimated evaporation boundary at $\sim 1800 \text{ K}$.

The average distance $\sqrt{r^2}$ corresponds to the radius determined by the vaporization boundary and is defined by the ratio: $\sqrt{r^2} \approx r_{\text{vapor}} = R \sqrt{T_a - T_{\text{vapor}}/T_a - T_w}$, where T_{vapor} corresponds to the phase transformation temperature, i.e. $\sim 1800 \text{ K}$ (figure 3). The carbon diffusion coefficients $D_{0(\text{C/C}_2)}$ at $T_0 = 273 \text{ K}$ were estimated to be [55]

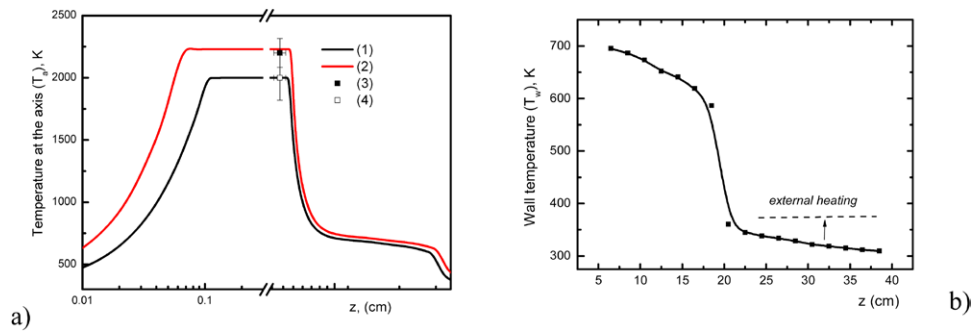


Figure 4. Axial distribution of (a) temperature at the axis (1)— $P = 500$ W, (2)— $P = 900$ W, (3)—exp. $P = 500$ W, (4)—exp. $P = 900$ W; and (b) the wall temperature along the discharge and remote plasma (points—experiment; solid line—fitting curve). The change in the wall temperature due to external heating is shown by a broken curve.

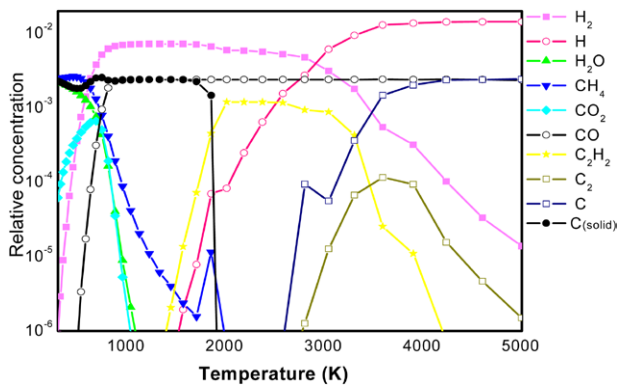


Figure 5. Simplified equilibrium diagram for the main ethanol decomposition products for $Q_{Et} = 0.6$ sccm and $Q_{Ar} = 250$ sccm.

$$D_{0(C/C_2)} = \frac{4}{3} \left(\frac{2}{\pi} \right)^{3/2} \frac{(k_B T_0)^{3/2}}{(d_{Ar} + d_{C/C_2})^2 M_{C/C_2}^{1/2} p} \approx a_{C/C_2} \times 1.7 \cdot 10^{-5} \text{ m}^2 \text{ s}^{-1}.$$

Here, the factor a_{C/C_2} is $a_{C/C_2} = 1$ for C, and $a_{C/C_2} = 0.707$ for C₂; M_{C/C_2} is the carbon atom/molecule mass in kg; p is the pressure in Pa at 273 K; k_B is the Boltzmann's constant; and d_{Ar} , d_{C/C_2} are the effective gas-dynamic diameters of the argon and carbon atoms/molecules in m, respectively. Finally, an approximate expression for the rate constant of gas phase carbon transformation into solid carbon was found:

$$k_{est} = a_{C/C_2} k_0 \cdot \left(\frac{T}{273} \right)^{3/2} \approx a_{C/C_2} 20 \left(\frac{T}{273} \right)^{3/2}. \quad (5)$$

In order to test the estimated coefficient k_{est} , the set of equations was solved by adopting the factor k_0 as a free parameter, to obtain a good fit with the experimental results. The best fit was obtained for $k_0 = 24$, which was very close to the estimated diffusion rate coefficient of carbon species (equation (5)). Therefore, the initial assumption of the diffusion nature of carbon transport is correct. The discrepancy can be attributed both to experimental errors and some inaccuracy of the estimation.

The system of equations described above was solved in a self-consistent manner yielding an integral description of

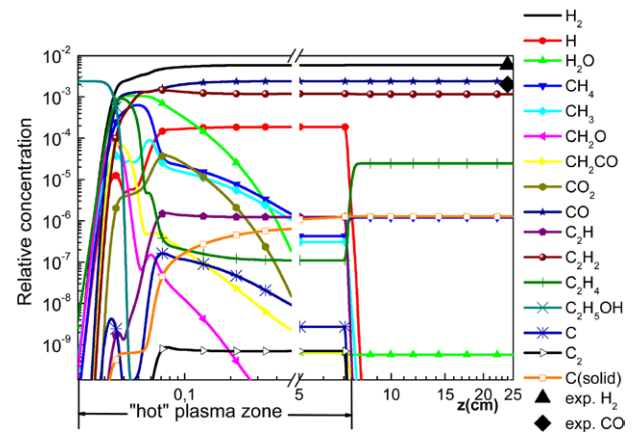


Figure 6. Evolution of main species concentrations in the discharge and the afterglow plasma for $Q_{Et} = 0.6$ sccm, $Q_{Ar} = 250$ sccm and $P = 900$ W.

the axial structure of the discharge and of the outlet plasma/gas stream. The algorithm used for the calculations is similar to that of the well-known computer code Reaction Design, Chemkin [48].

4. Results and discussion

The equilibrium values of the stable substances and intermediate complexes along the hot plasma zone were useful to understand the general workings of ethanol decomposition and formation of carbon precursors. The calculated equilibrium values, i.e. the calculated concentrations of the stable substances such as hydrogen, carbon oxide, water, and some intermediate complexes, are shown in figure 5 as a function of the gas temperature. It should be noted that the processes of formation of solid carbon were also taken into consideration.

Four temperature regions can be distinguished. The first region is up to ~1000 K where the presence of methane is observed. The second region ranges from 1000 to 2000 K, with formation of solid carbon and H₂. The third region is from 2000 to 3500 K. In this region H₂ is still dominant while acetylene is also present in significant concentration. Finally, for temperatures above 3500 K, a complete decomposition of H₂ and C₂ leading to the formation of carbon in gas phase and atomic hydrogen is observed. The theoretical results

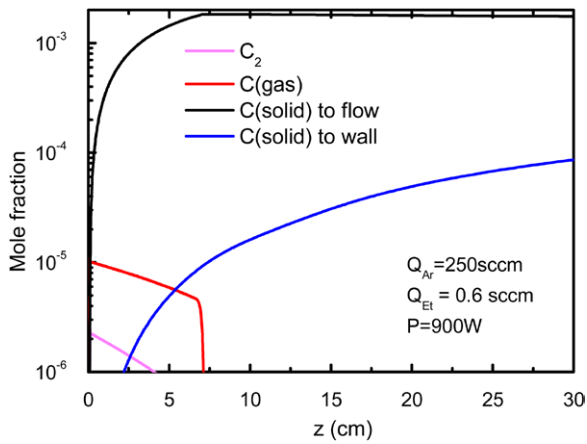


Figure 7. Axial distribution of total carbon–dicarbon relative density.

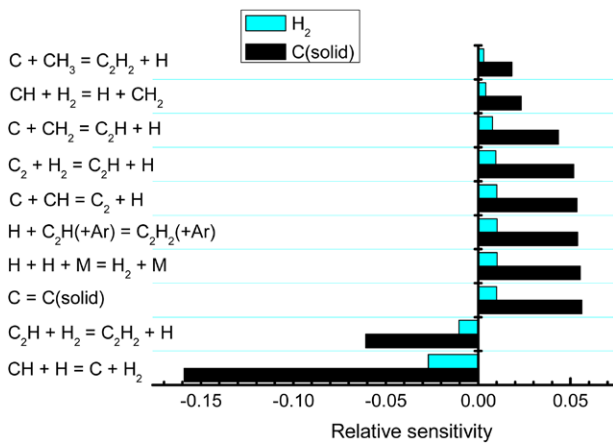


Figure 8. Results of sensitivity analysis for the chemical reactions on the formation of H₂ and C (solid). $P = 900$ W, $Q_{Ar} = 250$ sccm, $Q_{Et} = 0.6$ sccm.

presenting the axial distribution of the decomposition products for heterogeneous case (gas + solid phase) are shown in figure 6. Ethanol dissociation begins in the hot plasma zone at temperatures of ~ 1000 – 1500 K (~ 0.5 cm).

The analysis of both modeling results and the rate coefficients allowed us to conclude that the ethanol decomposition can occur through two parallel channels with equal probability (see figure 3). According to the first channel, the single bond C–C is broken to form CH₂OH and CH₃ radicals. Further, CH₂OH is decomposed into the complexes CH₂O and HCO and finally into CO and H. In a second channel, an OH group is detached from the ethanol molecule, followed by the formation of double C = C bond in the C₂H₄ molecule and further a triple C \equiv C bond in the C₂H₂ molecule. Acetylene is a stable molecule and can be broken down to the simplest C and H at sufficiently high temperatures (above 4000 K). However, diffusion of gas-phase carbon takes place from the hot plasma zone towards the tube wall, where the temperature is lower and where the nucleation of carbon species takes place. The described processes and chemical reaction mechanisms are schematically illustrated in figure 3.

The main zone, where nucleation occurs, is located near the tube walls. In figure 3 this is the zone outside of the vaporization

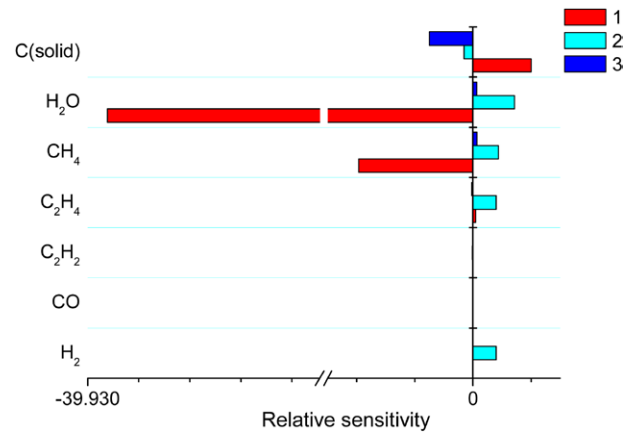


Figure 9. Sensitivity analysis of the main gas products' dependence on (1) microwave power P , (2) additional hydrogen gas in the background gas mixture, and (3) argon flow rate Q_{Ar} . ($P = 900$ W, $Q_{Ar} = 250$ sccm, $Q_{Et} = 0.6$ sccm.)

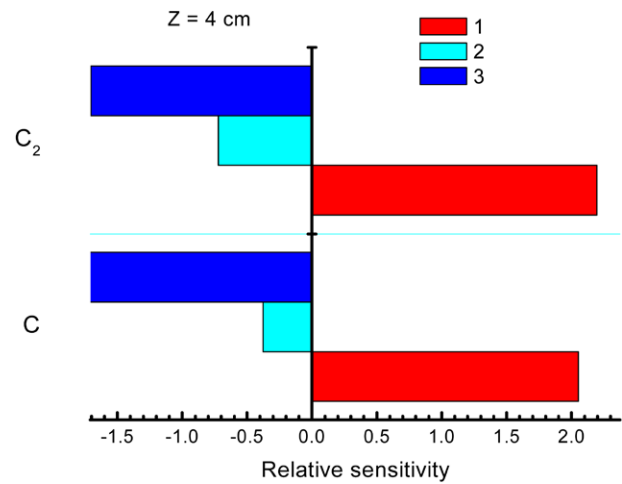


Figure 10. Sensitivity analysis of the C and C₂ (in a hot plasma zone at axial distance $z = 4$ cm) dependence on (1) microwave power P , (2) additional hydrogen gas in the background gas mixture, and (3) argon flow rate Q_{Ar} . ($P = 900$ W, $Q_{Ar} = 250$ sccm, $Q_{Et} = 0.6$ sccm.)

boundary surface. The main outlet gas products of ethanol decomposition are CO and H₂. Acetylene and ethylene are also present in very small amounts, i.e. less than 0.1% (figure 6). A fraction of the solid carbon nuclei accumulates on the wall, but the majority of it is gradually removed with the outlet gas stream in the assembly zone as seen in figure 7.

In order to evaluate the relative contribution of the different chemical reactions for solid carbon and H₂ production, a sensitivity analysis was performed. For this purpose, the relative sensitivity to the rate coefficients has been calculated and shown in figure 8. The relative sensitivity is defined as [44]

$$S_{i,r}^{\text{rel}} = \frac{k_r}{c_i} \frac{\partial c_i}{\partial k_r} = \frac{\partial \ln c_i}{\partial \ln k_r}, \quad (6)$$

where k_r are the rate coefficients of the elementary reactions and c_i are the concentrations of the species.

The analysis results indicate that the most important reactions that influence the H₂ production also influence the solid carbon production. The absolute difference between H₂ and

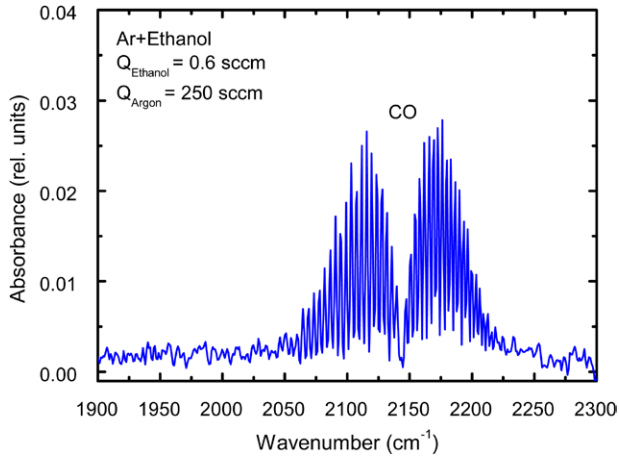


Figure 11. Infrared absorption spectra of outlet gas stream as detected by an FT-IR spectrometer.

solid carbon sensitivity coefficients is due to the fact that part of the hydrogen is generated by the first channel and does not depend on the carbon diffusion velocity, while the solid carbon is only determined by the second channel. Additionally, solid carbon formation does not occur through the CO generation mechanism. The latter only occurs through the first channel of ethanol decomposition and does not depend on the carbon diffusion velocity.

The relative sensitivities of different stable species as functions of three different externally controlled parameters, such as microwave power P delivered to the launcher, hydrogen percentage in the background gas mixture C_{H_2} and argon flow rate Q_{Ar} were evaluated as follows:

$$\begin{aligned} S(P)_i^{\text{rel}} &= \frac{P}{c_i} \frac{\partial c_i}{\partial P} = \frac{\partial \ln c_i}{\partial \ln P}, \\ S(C_{H_2})_i^{\text{rel}} &= \frac{C_{H_2}}{c_i} \frac{\partial c_i}{\partial C_{H_2}} = \frac{\partial \ln c_i}{\partial \ln C_{H_2}}, \\ S(Q_{Ar})_i^{\text{rel}} &= \frac{Q_{Ar}}{c_i} \frac{\partial c_i}{\partial Q_{Ar}} = \frac{\partial \ln c_i}{\partial \ln Q_{Ar}} \end{aligned} \quad (7)$$

where c_i is the species concentration.

Increasing the microwave power P leads to an increase of the solid carbon production rate but does not affect the generation of H_2 and CO (figure 9). The same reactions influence both H_2 and solid carbon production, according to the analysis. However, the formation of H_2 and CO occurs via the first channel and does not depend on the carbon diffusion velocity, while solid carbon formation is determined only by the second channel (figure 3). When additional hydrogen gas is injected into the microwave plasma, the total solid carbon yield decreases (figure 10). The addition of H_2 shifts the equilibrium towards the formation of acetylene and ethylene from C_2 . More hydrogen in the plasma results in increasing of H and OH radical densities. The reactions of these radicals with carbon atoms and molecules result in decreasing carbon species densities. Finally, an increase of the Ar flow rate will also lead to a decrease in solid carbon generation, due to the decrease of ethanol's residence time in the plasma. The precursor (ethanol molecules) spent less time in the hot plasma

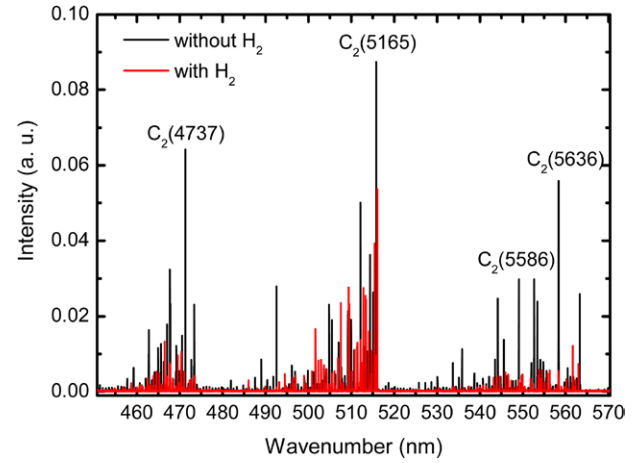


Figure 12. Emission spectra of Ar/ethanol plasma with and without additional H_2 flux ($z \approx 4$ cm, $P = 900$ W, $Q_{Ar} = 250$ sccm, $Q_{Et} = 0.6$ sccm, $Q_{H_2} = 2.5$ sccm).

zone, and the gas phase carbon species fails to diffuse towards the nucleation zone.

The model predictions were validated with experimental results obtained by emission, Fourier transform infrared (FT-IR) spectroscopy and mass spectrometry techniques. The result obtained by mass and FT-IR spectroscopy demonstrate that the main outlet gas products are H_2 and CO thus validating the theoretical results as seen in figure 6 (experimental points). Moreover, as shown in figure 11 the absorption peak of CO at ~ 2170 cm^{-1} is the only one detected, in accordance with the mass spectroscopy results.

Furthermore, the detected changes in emission spectra of the Swan system of molecular C_2 , between 4500 and 5700 Å ($A^3\Pi_g \rightarrow X^3\Pi_u$), when hydrogen gas is injected into the background gas mixture, are shown in figure 12. It can be seen that the intensity of C_2 lines decrease with addition of hydrogen. In our previous work [34] the emission of excited carbon atoms at 247.9 nm at higher concentration of ethanol precursor was detected. However, decreasing the ethanol precursor in the mixture decreased the intensity of this line, and it is difficult separate from the background noise. The emission spectra were detected from the active plasma zone at axial distance $z \approx 4$ cm.

The estimation of the relative change of the C_2 lines intensity (figure 12) due to the change in the hydrogen percentage in the gas mixture is given in table 2. The corresponding quantity is defined in the same manner as the sensitivity factors:

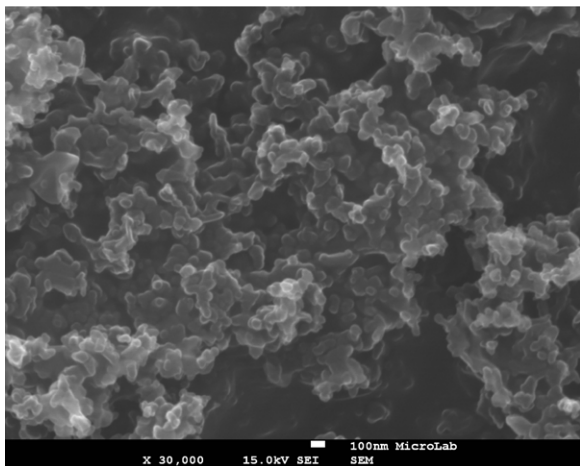
$$\begin{aligned} S(J)^{\text{rel}} &= \frac{Q_{H_2}}{J} \frac{\partial J}{\partial Q_{H_2}} \approx -\frac{1}{2} \left(\frac{Q_{H_2}^{\text{add}}}{3Q_{C_2H_5OH}} \times \frac{J_0 - J_{H_2}}{J_0} \right. \\ &\quad \left. + \frac{3Q_{C_2H_5OH} + Q_{H_2}^{\text{add}}}{Q_{H_2}^{\text{add}}} \times \frac{J_0 - J_{H_2}}{J_{H_2}} \right). \end{aligned} \quad (8)$$

Here J_0 and J_{H_2} are the spectral lines intensity without and with the addition of hydrogen gas.

The estimated values of the sensitivity factor using equation (8) are nearly equal to the ones obtained by the theoretical model (see figure 10), thus validating model predictions. The

Table 2. Estimation of the relative change of the C₂ line intensities with and without hydrogen addition.

Wavelength (nm)	473.7	516.5	558.6	563.6	Mean value	Standard deviation
$S(J)^{\text{rel}}$	-0.72	-0.69	-0.88	-2.43	-1.18	0.84

**Figure 13.** SEM image of solid carbon deposited on the tube wall: $P = 900\text{ W}$, $Q_{\text{Et}} = 0.6\text{ sccm}$, $Q_{\text{Ar}} = 250\text{ sccm}$.

minus sign implies that the intensity of the C₂ emission lines decreases.

As has already been discussed, under heterogeneous conditions (gas + solid carbon nuclei), the diffusion of carbon species into colder nucleation zones, both in radial and axial directions, takes place. Some part of the solid carbon is deposited on the tube wall (figure 13) while the main part is gradually withdrawn from the hot plasma region. Therefore, the main part of solid nuclei is transported with axial gas flow into the assembly zone where kinetic processes of growth and assembling of carbon nanostructures occur. These nanostructures are subsequently captured from the gas stream by a membrane filter. Final structure of the carbon nanostructure is a result of delicate interplay between carbon particles and energy fluxes as determined by the plasma and the conditions in the assembly zone. As shown in [27] the changes in thermodynamic conditions in the assembly zone by external forced cooling/heating results in a different final product, i.e. nanoparticles, sheets etc. This gives some confidence in our hypothesis that the growth processes take place in the postdischarge, i.e. assembly zone.

A SEM image of solid carbon residue deposited on the wall in the assembly zone of the plasma reactor is shown in figure 13. As seen, the synthesized material has amorphous structure with carbon clusters size of several nanometers. The carbon clusters have a quasispherical shape, i.e. nearly round primary particles, known as nodules, with a size of 50–300 nm. The nodules coalesce together to form aggregates.

A typical SEM image of the graphene sheets synthesized and captured by the filter membrane is shown in figure 14(a). This result is further confirmed by Raman spectroscopy measurements. The synthesized nanostructures were deposited on a glass substrate, and the Raman spectra from different regions on the substrate were obtained. As seen in figure 14(b), where typical Raman spectrum is shown, the sheets exhibit a sharp 2D peak at $\sim 2660\text{ cm}^{-1}$ due to the second-order process and

a G-band peak due to the tangential zone center mode at 1583 cm^{-1} , as well as disorder D-peak at 1331 cm^{-1} [28]. This type of Raman spectra has often been associated with graphene and provides evidence that the obtained nanosheets are indeed graphene. The $I_{2\text{D}}/I_{\text{G}}$ ratio of ~ 1.5 and the full width of half maximum of the 2D peak less than 50 cm^{-1} indicate that the sheets consist of just a few (one to five) monolayers.

To obtain more information about the structural quality of the assembled graphene sheets, XPS analysis was performed. An example of the survey XPS of the samples is presented in figure 15, on which the main photoelectron and Auger lines of carbon and oxygen can be clearly observed. Besides, small intensity Si lines from the substrate are also present due to the tape used to peel the carbon material from the filters.

Results of the detailed analysis of the C 1s line are presented in figure 16. The dominant contribution in the C 1s line peak was attributed to sp² carbon at 284.4 eV, which was used as a reference for the energy axis calibration. Accordingly, the line was fitted to six different contributions attributed to sp² carbon (at 284.4 eV), sp³ carbon (at 285.1 eV), presence of a satellite due to the $\pi-\pi^*$ excitation and carbon in different carbon–oxygen bonds (see figure 16). The latter were also identified in the O 1s line and originate from the sample contamination. Introducing additional H₂ in the gas mixture does not affect significantly the relative amounts of carbon–oxygen bonds as seen from the results shown in table 3. However, the amount of oxygen attached to the nanostructure scaffolds has nearly doubled in respect to the results in Tatarova *et al* [28] obtained for the same argon and ethanol partial fluxes but with 900 W of applied microwave power. The obtained C/O atomic ratio in Tatarova *et al* [28] is 18.4. As shown by theoretical calculations, the number density of strongly reactive OH radicals in the hot plasma and in the near afterglow increases with the injection of H₂ and can contribute to an increase in oxygen functionalities of the graphene sheets.

Furthermore, addition of H₂ in the carrier gas increases the sp³/sp² ratio from 0.47 ($Q_{\text{H}_2} = 1\text{ sccm}$) to 0.52 ($Q_{\text{H}_2} = 2.5\text{ sccm}$) (table 3). Therefore, the relative amount of sp³ carbons increases (see table 3). By comparison, the sp³/sp² ratio obtained in [28] is only 0.25. Therefore, a correlation between changes in C₂ and C number densities and sp³/sp² ratio can be found. As has already been noted, the densities of H and OH radicals in plasma zone increase when H₂ is added. The reactions involving these radicals with carbon atoms and molecules strongly reduce the solid carbon output, as shown by sensitivity analysis (see figure 10). However, the effect of additional H₂ is two times stronger in the production of C₂ radical than in the production of C atoms (figures 10 and 12). The observed correlation gives some confidence in the hypothesis that the assembling of planar sp² carbons is ruled mainly by the presence of C₂ radicals in the carbon seeds [57]. Inversely, an increase of carbon atoms in the seeds leads to an increase in the synthesis of sp³ carbon.

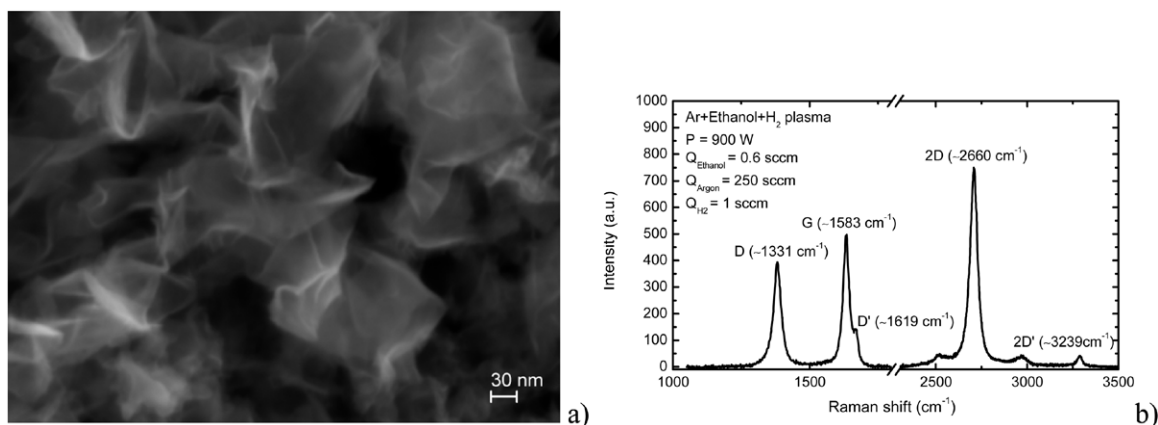


Figure 14. (a) SEM image of the graphene sheets captured by a membrane filter; (b) Raman spectrum of the sheets ($P = 900$ W, $Q_{Et} = 0.6$ sccm, $Q_{Ar} = 250$ sccm, $Q_{H_2} = 1$ sccm).

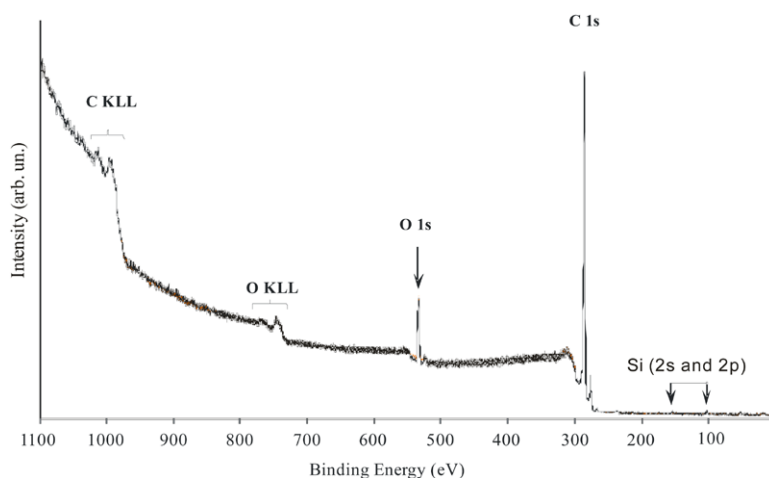


Figure 15. Survey XPS spectrum of the sample obtained at $P = 700$ W. The background gas mixture is $Q_{Ar} = 250$ sccm, $Q_{Et} = 0.6$ sccm and $Q_{H_2} = 2.5$ sccm.

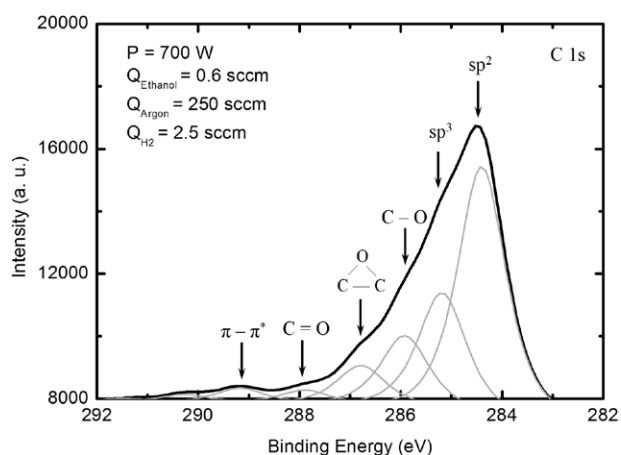


Figure 16. Detailed spectra of the C 1s region of the XPS spectrum.

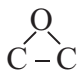
5. Conclusions

Experimental and theoretical studies on the synthesis of carbon nanostructures, and in particular of freestanding graphene sheets, applying microwave plasma at 2.45 GHz and atmospheric pressure have been conducted. The procedure involved

the introduction of ethanol vapor into a microwave argon plasma environment, where decomposition of ethanol molecules took place and solid carbon was created. The accumulation of solid carbon residue on the discharge tube wall at the assembly zone of the plasma reactor was observed. The solid assembled from the main stream, which was gradually withdrawn from the hot plasma region in the outlet plasma stream directed to a filter, was composed of flowing graphene sheets.

Aiming at further elaboration of the method and replacement of the phenomenological approach with a deterministic one, a theoretical model previously developed was updated and refined to describe in detail the formation of carbon precursor species and solid carbon nuclei. Taking into consideration that the nucleation process is an interplay between thermodynamic and kinetic factors, the model is based on a set of nonlinear spatially dependent differential equations describing plasma thermodynamics and chemical kinetics. Considering the diffusion of carbon species into colder zones of the plasma reactor, the formation of solid carbon nuclei in the colder nucleation zones of plasma reactor was analyzed in detail. Hydrogen, carbon monoxide and solid carbon were identified as the main products of ethanol decomposition in the argon plasma, as predicted by the model and

Table 3. Peak positions, corresponding assignment and relative amounts of carbon (C 1s) and oxygen (O 1s) atoms of carbon nanostructures at different percentage of H₂ gas in the background gas mixture.

Samples	BE (± 0.2 eV)		Assignment	At conc. (%)	
	1	2		H ₂ (2.5 sccm)	H ₂ (1 sccm)
C 1s	284.4	284.4	sp ² carbon	45.4	47.1
	285.1	285.2	sp ³ carbon	23.6	22.0
	285.8	285.9	C–O	14.2	13.3
	286.7	286.8		6.8	7.2
	287.6	287.9	O–C–O or C=O	2.7	2.4
O 1s	532.4	532.3	aliphatic C=O	3.9	3.9
	533.9	533.9	O–C=O or –OC–O–CO–	3.6	4.0
			C sp ³ /C sp ²	0.52	0.47
C/O			12.4	11.6	

experimentally confirmed. The ethanol decomposition begins in the hot plasma zone, at temperatures of ~1000–1500 K, and occurs via two simultaneously running channels with equal probability: the first channel leads to the formation of carbon monoxide and H₂, while the second one leads to the formation of gas-phase carbon, ethylene and acetylene. Gas-phase carbon atoms/molecules diffuse into colder nucleation zones, both in radial and axial directions, resulting in gas-phase carbon transformation into solid carbon nuclei. The generation of solid carbon was determined by the second decomposition channel and did not depend on CO formation. The model predictions for the main outlet gas products, i.e. CO and H₂, were validated with the experimental results obtained by mass and FT-IR spectroscopy. These results constitute strong proof of the reliability of the approach used. Given the fact that a self-consistent problem is solved (small change in one of the parameters results in change of all other parameters and final results), the model provides reliable description of the system under investigation, and the output results can be further used as input data for molecular dynamics simulations.

The influence of additional hydrogen in the background gas mixture, i.e. Ar/C₂H₅OH/H₂ ratio on the carbon precursor (C₂, C) densities, and on the structural quality of fabricated graphene sheets was analyzed. A correlation between changes in C₂ and C number densities and sp³/sp² ratio was found. The densities of H and OH radicals in the plasma zone increased with the addition of H₂. The reactions involving these radicals and carbon atoms and molecules strongly reduce the solid carbon output as shown by the sensitivity analysis. The influence of additional H₂ was, by a factor of two, stronger on the production of a C₂ radical than on C atoms. A correlation between the reduction of C₂ emissions and the sp³/sp² carbon ratio increase in the graphene sheets was observed. This result provided some confidence in the hypothesis that the assembly of planar sp² carbons was dominated by the presence of C₂ radicals in the carbon seeds, while more carbon atoms in the seeds resulted in more sp³ carbon synthesis.

Additional work should be done to relate the plasma-specific properties/features and specific structural qualities of assembled nanostructures that in turn determine their electronic, mechanical, photonic, etc properties. The results on

carbon precursor's fluxes will be further used as input data for mechanistic models to simulate the nucleation and growth processes of carbon nanostructures. Furthermore a detailed analysis of the carbon balance, considering carbon deposited on the wall and the solid-phase carbon withdrawn with the plasma gas flow, should be carried out. The results of such investigations will be reported in a future work.

Acknowledgments

This work was funded by Portuguese FCT—Fundação para a Ciência e a Tecnologia, under Project UID/FIS/50010/2013, Project INCENTIVO/FIS/LA0010/2014, and grant SFRH/BD/52413/2013 (PD-F APPLAuSE).

References

- [1] Ostrikov K, Cvelbar U and Murphy A B 2011 *J. Phys. D: Appl. Phys.* **44** 174001
- [2] Novoselov K S, Geim A K, Morosov S V, Jiang D, Zhang Y, Dubonos S V, Grigorieva I V and Firsov A A 2004 *Science* **306** 666–9
- [3] Tatarova E, Bundaleska N, Sarrette J Ph and Ferreira C M 2014 *Plasma Sources Sci. Technol.* **23** 063002
- [4] Yurum Y, Taralp A and Veziroglu N 2009 *Int. J. Hydrogen Energy* **34** 3784
- [5] Ostrikov K, Neyts E C and Meyyappan M 2013 *Adv. Phys.* **62** 113–224
- [6] Choi H, Jung S, Seo J, Chang D W, Dai L and Baek J 2012 *Nano Energy* **1** 534
- [7] Wu Y H, Yu T and Shen Z X 2010 *J. Appl. Phys.* **108** 071301
- [8] Gonzalez-Aguilar J, Moreno M and Fulcheri L 2007 *J. Phys. D: Appl. Phys.* **40** 2361–74
- [9] Phillips J, Luhrs C C and Richard M 2009 *IEEE Trans. Plasma Sci.* **37** 726
- [10] Levchenko I, Keidar M, Xu S, Kersten H and Ostrikov K 2013 *J. Vac. Sci. Technol. B* **31** 050801
- [11] Geim A K and Novoselov K S 2007 *Nat. Mater.* **6** 183–91
- [12] Zhang Y B, Tan Y W, Stormer H L and Kim P 2005 *Nature* **438** 201–4
- [13] Neto A H C, Guinea F, Peres N M R, Novoselov K S and Geim A K 2009 *Rev. Mod. Phys.* **81** 109–62

- [14] Iijima S 1991 *Nature* **354** 56–8
- [15] Gusev A I 2007 *Nanomaterialy, Nanostruktury, Nanotekhnologii* (*Nanomaterials, Nanostructures, Nanotechnology*) (Dordrecht: Springer) FIZMATLIT 416 (in Russian)
- [16] Tsyganov D L 2005 Deposition carbonic and diamond-like films by means of plasma jets Moscow Aviation Institute *PhD Thesis* State University of Aerospace Technologies p 159 (in Russian)
- [17] Kumar Sh, Levchenko I, Ostrikov K and McLaughlin J A 2012 *Carbon* **50** 321–41
- [18] Sazonov M I and Tsyganov D L 2005 *Instrum. Exp. Tech.* **48** 266–9
- [19] Chou C H and Phillips J 1992 *J. Mater. Res.* **7** 2107
- [20] Phillips J, Shim S, Fonseca I M and Carabineiro S 2002 *Appl. Catal.* **237** 41
- [21] Chen C K, Perry V W and Phillips J 2002 *Carbon* **41** 2555
- [22] Lambert T N, Luhrs C C, Chavez C A, Wakeland S, Brumbach M T and Alam T M 2010 *Carbon* **48** 4081
- [23] Luhrs C, Wakeland S and Carpenter B 2012 Graphene, graphitic and amorphous carbon nanostructures generation by atmospheric microwave plasma method *Plasma for Environmental Issues* ed E Tatarova et al (Sofia: Artgraf) pp 69–80
- [24] Garaj S, Hubbard W and Golovchenko J A 2010 *Appl. Phys. Lett.* **97** 183103
- [25] Yamada T, Kim J, Ishihara M and Hasegawa M 2013 *J. Phys. D: Appl. Phys.* **46** 063001
- [26] Nandamuri G, Roumimov S and Solanki R 2010 *Appl. Phys. Lett.* **96** 154101
- [27] Tatarova E, Henriques J P, Luhrs C C, Dias A, Phillips J, Abrashev M V and Ferreira C M 2013 *Appl. Phys. Lett.* **103** 134101
- [28] Tatarova E, Dias A, Henriques J, Botelho de Rego A, Ferraria A, Abrashev M, Luhrs C C, Phillips J, Dias F M and Ferreira C M 2014 *J. Phys. D: Appl. Phys.* **47** 385501
- [29] Bogaerts A, Eckert M, Mao M and Neyts E 2011 *J. Phys. D: Appl. Phys.* **44** 174030
- [30] Choi H S, Kim K H, Hong K-H, Kim J, Lee H S, Shin J K, Vasenkov A V, Fedoseyev A I and Kolobov V 2005 *NSTI-Nanotechnol.* **2** 185–8
- [31] Vasenkov A V, Fedoseyev A I, Kolobov V I, Choi H S, Hong K-H, Kim K, Kim J, Lee H S and Shin J K 2006 *J. Comput. Theor. Nanosci.* **13** 453–8
- [32] Pannala S and Wood R F 2004 *J. Nanosci. Nanotechnol.* **1** 4 463–70
- [33] Moisan M and Zakrzewski Z 1991 *J. Phys. D: Appl. Phys.* **24** 1025
- [34] Tsyganov D, Bundaleska N, Tatarova E and Ferreira C M 2013 *Int. J. Hydrogen Energy* **38** 14512–30
- [35] Marinov N M 1999 *J. Chem. Kinet.* **31** 183–220
- [36] GRI-Mech© Version 3.0 7/30/99 www.gri.org
- [37] Konnov A 2000 Detailed reaction mechanism for small hydrocarbons combustion, Release 0.5, <http://homepages.vub.ac.be/~akonnov/>
- [38] Marinov N M and Malte P C 1995 *Int. J. Chem. Kinet.* **27** 957–86
- [39] Marinov N M, Pitz W J, Westbrook C K, Vincitore A M, Castaldi M J, Senkan S M 1998 *Combust. Flame* **114** 192–213
- [40] Tsang W and Hampson R F 1986 *J. Phys. Chem. Ref. Data* **15** 1087–279
- [41] Smith G P, Park C, Schneiderman J and Luque J 2005 *Combust. Flame* **141** 66–77
- [42] Tsyganov D 2013 *High Temp.* **51** 1
- [43] Glassman I 1996 *Combustion* 3rd edn (New York: Academic) p 631
- [44] Warnatz J, Maas U and Dibble R W 2006 *Physical and Chemical Fundamentals, Modeling and Simulation, Experiments, Pollutant Formation* 4th edn (Berlin: Springer) p 378
- [45] NIST© ‘Real Fuels’ Detailed Chemical Kinetic Combustion Model Database, <http://kinetics.nist.gov/realfuels>
- [46] Goos E, Burcat A and Ruscic B 2001 Third millennium ideal gas and condensed phase thermochemical database for combustion, Haifa, Israel *Technion Aerospace Engineering Report #867*, <ftp://ftp.technion.ac.il/pub/supported/aetddd/thermodynamics> (January 2005 update)
- [47] Allendorf M D and Besmann T M *High Temperature Thermodynamics Database* Sandia National Laboratories www.ca.sandia.gov/HiTempThermo/
- [48] Reaction design, chemkin thermochemical database, <http://reactiondesign.com>
- [49] Tatarova E, Dias F M, Felizardo E, Henriques J, Pinheiro M J, Ferreira C M and Gordiets B 2010 *J. Appl. Phys.* **108** 123305–18
- [50] Henriques J, Bundaleska N, Tatarova E, Dias F M and Ferreira C M 2011 *Int. J. Hydr. Energy* **36** 345–54
- [51] Henriques J, Tatarova E, Guerra V and Ferreira C M 2002 *J. Appl. Phys.* **91** 5622
- [52] Tatarova E et al 2012 *J. Appl. Phys.* **112** 093301–14
- [53] Henriques J, Tatarova E and Ferreira C M 2011 *J. Appl. Phys.* **109** 023301
- [54] Henriques J, Tatarova E, Dias F M and Ferreira C M 2011 *J. Appl. Phys.* **109** 023302
- [55] Biberman L M, Vorob’ev V S and Aikubov I T 1987 *Kinetics of Nonequilibrium Low-Temperature Plasmas* (New York: Consultants Bureau)
- [56] Landau L D, Lifshitz E M and Pitaevskii L P 1981 *Physical kinetics Course of Theoretical Physics* vol 10, Reprint edn (Oxford: Pergamon) p 452
- [57] Endo M and Kroto H W 1992 *J. Phys. Chem.* **96** 6941